Journal of Computational Physics 479 (2023) 111987

Contents lists available at ScienceDirect

Journal of Computational Physics

journal homepage: www.elsevier.com/locate/jcp

Stochastic Galerkin method for cloud simulation. Part II: A fully random Navier-Stokes-cloud model

A. Chertock [a], A. Kurganov [b], M. Lukáčová-Medvid'ová [c,*], P. Spichtinger [d], B. Wiebe [e]

[a] Department of Mathematics, North Carolina State University, United States of America
[b] Department of Mathematics, SUSTech International Center for Mathematics and Guangdong Provincial Key Laboratory of Computational Science and Material Design, Southern University of Science and Technology, Shenzhen, 518055, China
[c] Institute of Mathematics, Johannes Gutenberg-University Mainz, Germany
[d] Institute of Atmospheric Physics, Johannes Gutenberg-University Mainz, Germany
[e] Institute of Mathematics, University of Zurich, Switzerland

ARTICLE INFO

Article history:
Received 13 April 2022
Received in revised form 15 January 2023
Accepted 31 January 2023
Available online 8 February 2023

Keywords:
Uncertainty quantification
Navier-Stokes equations
Stochastic Galerkin method
Finite-volume schemes
IMEX time discretization
Cloud dynamics

ABSTRACT

This paper is a continuation of the work presented in Chertock et al. (2019) [8]. We study uncertainty propagation in warm cloud dynamics of weakly compressible fluids. The mathematical model is governed by a multiscale system of PDEs in which the macroscopic fluid dynamics is described by a weakly compressible Navier-Stokes system and the microscopic cloud dynamics is modeled by a convection-diffusion-reaction system. In order to quantify uncertainties present in the system, we derive and implement a generalized polynomial chaos stochastic Galerkin method. Unlike the first part of this work, where we restricted our consideration to the partially stochastic case in which the uncertainties were only present in the cloud physics equations, we now study a fully random Navier-Stokes-cloud model in which we include randomness in the macroscopic fluid dynamics as well. We conduct a series of numerical experiments illustrating the accuracy and efficiency of the developed approach.

© 2023 The Authors. Published by Elsevier Inc. This is an open access article under the CC BY license (http://creativecommons.org/licenses/by/4.0/).

1. Introduction

In this paper, we continue the study of generalized polynomial chaos (gPC) stochastic Galerkin methods for multiscale cloud dynamics with uncertainty. The gPC expansion based methods, such as stochastic Galerkin [8,10,24,26,27,31] and stochastic collocation [20,28,30], are well-known techniques for uncertainty quantification in physical and engineering applications. In the context of fluid flow problems, the uncertainty quantification methods based on the gPC expansion were studied in, e.g., [16,18,19]. In [11], the stochastic Galerkin and stochastic collocation methods were compared, and it was shown that for simple problems the stochastic Galerkin methods can lead to more accurate approximation when using the same number of degrees of freedom. Theoretical analysis of these methods has been conducted in particular for elliptic or parabolic problems; see, e.g., [29,30] and the references therein. For transport-dominanted or hyperbolic problems we refer to, e.g., [2,3,12,13,17,23] and the references therein.

* Corresponding author.
E-mail addresses: chertock@math.ncsu.edu (A. Chertock), alexander@sustech.edu.cn (A. Kurganov), lukacova@uni-mainz.de (M. Lukáčová-Medvid'ová), spichtin@uni-mainz.de (P. Spichtinger), bettina.wiebe@math.uzh.ch (B. Wiebe).

https://doi.org/10.1016/j.jcp.2023.111987
0021-9991/© 2023 The Authors. Published by Elsevier Inc. This is an open access article under the CC BY license (http://creativecommons.org/licenses/by/4.0/).

In gPC expansion based methods, the solution is approximated by a truncated generalized Fourier series in terms of orthogonal polynomials corresponding to the underlying probability density function. The stochastic collocation method belongs to the class of *non-intrusive methods* in which the original deterministic system is solved at certain collocation points in the stochastic space, and then the gPC coefficients are obtained by using a polynomial interpolation and a suitable numerical quadrature. The stochastic Galerkin method on the other hand is an *intrusive method* in which the Galerkin projection is employed after substituting the gPC expansions into the original system. This leads to a larger coupled system of deterministic PDEs for the gPC coefficients for which an accurate and efficient numerical method is to be developed.

The multiscale cloud model we study is governed by a coupled macro-microscopic Navier-Stokes-cloud system with random data and parameters. In the first part of this work [8], we restricted our consideration to the partially stochastic case in which the uncertainties were only present in the cloud physics equations keeping the fluid dynamics deterministic. For that model, we have developed an operator splitting approach in which the deterministic macroscopic Navier-Stokes equations were solved numerically by an implicit-explicit (IMEX) asymptotically preserving (AP) finite-volume method, while the stochastic microscopic cloud dynamics were solved by a gPC expansion. The latter was realized by the stochastic Galerkin method combined with an explicit finite-volume approximation for the system of gPC coefficients. The coupling of the deterministic Navier-Stokes equations with the stochastic cloud dynamics was realized by using expected values for the coupling source terms.

In the present work, we extend the gPC stochastic Galerkin (gPC-SG) method from [8] to a fully coupled random multiscale Navier-Stokes-cloud model where we include randomness in the macroscopic fluid dynamics as well. Consequently, the random coupling source terms will be considered. This will result in deterministic PDEs for the gPC coefficients representing both Navier-Stokes and cloud dynamics. The gPC coefficients for the fluid dynamics will be approximated by using an IMEX AP finite-volume method similar to the one used for the deterministic Navier-Stokes system. The gPC coefficients for the cloud dynamics will be computed by an adaptation of the explicit finite-volume developed in [8].

The present paper is organized as follows. For the consistency of presentation, we start in §2 with a short recap of the deterministic multiscale Navier-Stokes-cloud model and then introduce a fully random cloud model. The numerical method for the latter is presented in §3, which is followed by numerical experiments in §4. We demonstrate the experimental convergence of the developed method as well as its applicability for uncertainty quantification in atmospheric flows through well-known meteorological benchmark tests of a rising warm and moist bubble and Rayleigh-Bénard convection.

2. Mathematical model

We consider a mathematical model of cloud dynamics, which is based on the weakly compressible nonhydrostatic Navier-Stokes equations for moist atmosphere (that is, a mixture of ideal gases such as dry air and water vapor),

$$\begin{aligned}
&\rho_t + \nabla\cdot(\rho\boldsymbol{u}) = 0,\\
&(\rho\boldsymbol{u})_t + \nabla\cdot\Big(\rho\boldsymbol{u}\otimes\boldsymbol{u} + p\,\mathrm{Id} - \mu_m\rho\Big(\nabla\boldsymbol{u} + (\nabla\boldsymbol{u})^\top\Big)\Big) = -\rho g\boldsymbol{e_d},\\
&(\rho\theta)_t + \nabla\cdot(\rho\theta\boldsymbol{u} - \mu_h\rho\nabla\theta) = S_\theta,
\end{aligned} \tag{2.1}$$

and evolution equations for cloud variables,

$$\begin{aligned}
&(\rho q_v)_t + \nabla\cdot\big(\rho q_v\boldsymbol{u} - \mu_q\rho\nabla q_v\big) = \rho(-C+E),\\
&(\rho q_c)_t + \nabla\cdot\big(\rho q_c\boldsymbol{u} - \mu_q\rho\nabla q_c\big) = \rho(C-A_1-A_2),\\
&(\rho q_r)_t + \nabla\cdot\big(-v_q\rho q_r\boldsymbol{e_d} + \rho q_r\boldsymbol{u} - \mu_q\rho\nabla q_r\big) = \rho(A_1+A_2-E).
\end{aligned} \tag{2.2}$$

Here, t is the time variable, $\boldsymbol{x} = (x_1,\ldots,x_d)\in\mathbb{R}^d$ is the space vector, ρ is the density, $\boldsymbol{u} = (u_1,\ldots,u_d)^\top$ is the velocity vector, θ is the moist potential temperature, p is the pressure, g is the acceleration due to gravity, μ_m is the dynamic viscosity, μ_h is the thermal conductivity, and μ_q is the cloud diffusivity. Furthermore, $\boldsymbol{e_d} = \boldsymbol{e_3} = (0,0,1)^\top$ and $\boldsymbol{e_d} = \boldsymbol{e_2} = (0,1)^\top$ in the three-dimensional (3-D) and two-dimensional (2-D) cases, respectively. The cloud variables representing the mass concentration of water vapor, cloud droplets and rain drops, q_v, q_c and q_r, respectively, are given by

$$q_\ell = \frac{\text{mass of the respective phase}}{\text{mass of dry air}} \quad \text{for} \quad \ell\in\{v,c,r\}.$$

The terms C and E represent phase changes between vapor and cloud water (droplets), and A_1 and A_2 represent collision processes, which leads to the formation of large droplets and thus precipitation, and v_q is the raindrop fall velocity.

Note that the systems (2.1) and (2.2) are coupled through the source term S_θ, which represents the impact of phase changes and is given by

$$S_\theta = \rho\frac{L\theta}{c_pT}(C-E).$$

For a detailed description of S_θ and the terms E, C, A_1, A_2 and v_q see [8]. The temperature T can be obtained from the moist adiabatic ideal gas equation

$$T = \frac{R}{R_m}\theta\left(\frac{p}{p_0}\right)^{R_m/c_p},$$

where $p_0 = 10^5$ Pa is the reference pressure at the sea level. In addition to the usual definition of a potential temperature, we use $R_m = (1 - q_v - q_c - q_r)R + q_v R_v$ with the ideal gas constant of dry air $R = 287.05\ J/(kg{\cdot}K)$, the gas constant of water vapor $R_v = 461.51\ J/(kg{\cdot}K)$ and the specific heat capacity of dry air for constant pressure $c_p = 1005\ J/(kg{\cdot}K)$. In order to close the system, we determine the pressure from the equation of state that includes moisture

$$p = p_0\left(\frac{R\rho\theta}{p_0}\right)^{\gamma_m} \quad \text{with} \quad \gamma_m = \frac{c_p}{c_p - R_m}. \tag{2.3}$$

We note that in the dry case, that is when $q_v = q_c = q_r = 0$, R_m reduces to R, $S_\theta = 0$ and the moist ideal gas equation as well as the moist equation of state becomes their dry analog.

Solving the Navier-Stokes equations (2.1) in a weakly compressible regime is known to trigger numerical instabilities due to the multiscale effects. We follow the approach typically used in meteorological models, where the dynamics of interest is described by a perturbation of a background state, which is the hydrostatic equilibrium. The latter expresses a balance between the gravity and pressure forces. Denoting by $\bar{p}$, $\bar{\rho}$, $\bar{\boldsymbol{u}} = \boldsymbol{0}$, $\bar{\theta}$ and $\overline{\rho\theta}$ the respective background state, the hydrostatic equilibrium satisfies

$$\frac{\partial \bar{p}}{\partial x_d} = -\bar{\rho}g, \quad S_\theta = 0,$$

where $\bar{p}$ is obtained from the equation of state (2.3)

$$\bar{p} = p(\overline{\rho\theta}) = p_0\left(\frac{R\overline{\rho\theta}}{p_0}\right)^{\gamma_m}. \tag{2.4}$$

Let p', ρ', $\boldsymbol{u}'$, θ' and $(\rho\theta)'$ stand for the corresponding perturbations of the equilibrium state, then

$$p = \bar{p} + p', \ \ \rho = \bar{\rho} + \rho', \ \ \theta = \bar{\theta} + \theta', \ \ \boldsymbol{u} = \boldsymbol{u}', \ \ \rho\theta = \bar{\rho}\bar{\theta} + \bar{\rho}\theta' + \rho'\bar{\theta} + \rho'\theta' = \overline{\rho\theta} + (\rho\theta)'.$$

The pressure perturbation p' is derived from (2.3) and (2.4) using the following Taylor expansion

$$p(\rho\theta) \approx p(\overline{\rho\theta}) + \frac{\partial p}{\partial(\rho\theta)}\left(\rho\theta - \overline{\rho\theta}\right) = \bar{p} + \gamma_m p_0\left(\frac{R\overline{\rho\theta}}{p_0}\right)^{\gamma_m}\frac{(\rho\theta)'}{\overline{\rho\theta}},$$

which results in

$$p' \approx \frac{\gamma_m p_0}{\overline{\rho\theta}}\left(\frac{R\overline{\rho\theta}}{p_0}\right)^{\gamma_m}(\rho\theta)'.$$

Thus, a numerically preferable perturbation formulation of the Navier-Stokes equations (2.1) reads

$$\begin{aligned}
&\rho'_t + \nabla\cdot(\rho\boldsymbol{u}) = 0,\\
&(\rho\boldsymbol{u})_t + \nabla\cdot\left(\rho\boldsymbol{u}\otimes\boldsymbol{u} + p'\,\mathrm{Id} - \mu_m\rho\left(\nabla\boldsymbol{u} + (\nabla\boldsymbol{u})^\top\right)\right) = -\rho' g\boldsymbol{e_d},\\
&(\rho\theta)'_t + \nabla\cdot(\rho\theta\boldsymbol{u} - \mu_h\rho\nabla\theta) = S_\theta.
\end{aligned} \tag{2.5}$$

Meteorological applications typically inherit several sources of uncertainty, such as model parameters, initial and boundary conditions. Consequently, stochastic models need to be designed to analyze the influence of uncertainties on the fluid and cloud dynamics. In general, there are different ways to represent and take into account model uncertainty. In this paper, we choose a widely used approach in which the uncertainty is described by random fields. To this end we define an abstract probability space (Γ, Σ, P) and denote by ω an event $\omega \in \Gamma$. We assume that the initial data depend on ω, that is,

$$\rho'\big|_{t=0} = \rho'(\boldsymbol{x}, 0, \omega), \quad (\rho\boldsymbol{u})\big|_{t=0} = (\rho\boldsymbol{u})(\boldsymbol{x}, 0, \omega) \quad \text{and} \quad (\rho\theta)'\big|_{t=0} = (\rho\theta)'(\boldsymbol{x}, 0, \omega)$$

for the fluid variables and

$$(\rho q_\ell)\big|_{t=0} = (\rho q_\ell)(\boldsymbol{x}, 0, \omega) \quad \text{with} \quad \ell \in \{v, c, r\}$$

for the cloud variables. Consequently, the solution at later time will also depend on ω, that is, we will have $\rho'(\boldsymbol{x}, t, \omega)$, $(\rho\boldsymbol{u})(\boldsymbol{x}, t, \omega)$, $(\rho\theta)'(\boldsymbol{x}, t, \omega)$ and $(\rho q_\ell)(\boldsymbol{x}, t, \omega)$ for $\ell \in \{v, c, r\}$, while the background states $\bar{p}$, $\bar{\rho}$, $\bar{\boldsymbol{u}} = \boldsymbol{0}$, $\bar{\theta}$ and $\overline{\rho\theta}$ are independent of ω.

Remark 2.1. The system parameters and boundary conditions could also depend on the random variable. Some of that cases were considered in our previous work [8], but in this paper we restrict our attention to the situation in which randomness arises in the initial data only.

3. Numerical scheme

In this section, we describe a gPC-SG method for the coupled system (2.5), (2.2). First, in §3.1 we derive a system for the gPC coefficients and then in §3.2 we describe a method used to numerically solve the resulting system.

3.1. System of gPC coefficients

In the gPC-SG setup, the solution is sought in the form of polynomial expansions

$$\begin{aligned}&\rho'(\boldsymbol{x},t,\omega)=\sum_{k=0}^{M}(\widehat{\rho'})_k(\boldsymbol{x},t)\Phi_k(\omega),\quad \rho\boldsymbol{u}(\boldsymbol{x},t,\omega)=\sum_{k=0}^{M}(\widehat{\rho\boldsymbol{u}})_k(\boldsymbol{x},t)\Phi_k(\omega),\\&(\rho\theta)'(\boldsymbol{x},t,\omega)=\sum_{k=0}^{M}(\widehat{(\rho\theta)'})_k(\boldsymbol{x},t)\Phi_k(\omega)\end{aligned}\tag{3.1}$$

and

$$\rho q_\ell(\boldsymbol{x},t,\omega)=\sum_{k=0}^{M}(\widehat{\rho q_\ell})_k(\boldsymbol{x},t)\Phi_k(\omega)\quad\text{with}\quad \ell\in\{v,c,r\},\tag{3.2}$$

where $\Phi_k(\omega)$, $k=0,\ldots,M$, are polynomials of degree k that are orthogonal with respect to the probability density function $\mu(\omega)$. Assuming that Γ is a compact metric event space, the corresponding Riemann integrals can be defined (see [25]), and then the orthogonality property implies

$$\langle\Phi_k,\Phi_{k'}\rangle:=\int_\Gamma\Phi_k(\omega)\Phi_{k'}(\omega)\mu(\omega)\,\mathrm{d}\omega=c_k\delta_{kk'}\quad\text{for}\quad 0\le k,k'\le M,\tag{3.3}$$

where $\delta_{kk'}$ is the Kronecker symbol and c_k are constants depending on the probability density function μ. In this work, we will focus on two distributions that are important for meteorological applications:

(1) A *uniform distribution* $\mathcal{U}(\Gamma)$ with $\Gamma=[-1,1]$, which corresponds to the Legendre polynomials

$$\Phi_k(\omega)=\sum_{j=0}^{\lfloor\frac{k}{2}\rfloor}(-1)^j\frac{(2k-2j)!}{(k-j)!(k-2j)!j!2^k}\omega^{k-2j},\quad\left\lfloor\frac{k}{2}\right\rfloor=\begin{cases}\frac{k}{2},&\text{if } k \text{ is even},\\ \frac{k-1}{2},&\text{if } k \text{ is odd},\end{cases}$$

which are orthogonal with respect to the probability density function $\mu(\omega)=1/2$ and the constants in (3.3) are $c_k=\frac{1}{2k+1}$.

(2) A *normal distribution* $\mathcal{N}(\mu_H,\sigma_H^2)$ with $\Gamma=(-\infty,\infty)$ which corresponds to the Hermite polynomials

$$\Phi_k(\omega)=2^{-\frac{k}{2}}H_k\left(\frac{\omega-\mu_H}{\sqrt{2}\sigma_H}\right)\quad\text{with}\quad H_k(\omega)=(-1)^k\boldsymbol{e}^{\omega^2}\frac{\mathrm{d}^k}{\mathrm{d}\omega^k}\left(e^{-\omega^2}\right),$$

where μ_H and σ_H are the mean value and the standard deviation, respectively. One can show that the Hermite polynomials Φ_k are orthogonal with respect to $\mu(\omega)=\frac{1}{\sqrt{2\pi\sigma_H^2}}\exp\left(-{}^{(\omega-\mu_H)^2}/_{(2\sigma_H^2)}\right)$ and the constants in (3.3) are $c_k=k!$.

Applying the Galerkin projection to (2.5) and (2.2) yields for $k=0,\ldots,M$

$$\begin{aligned}\left\langle(\rho')_t+\nabla\cdot(\rho\boldsymbol{u}),\Phi_k\right\rangle&=0,\\ \left\langle(\rho\boldsymbol{u})_t+\nabla\cdot\left(\rho\boldsymbol{u}\otimes\boldsymbol{u}+p'\mathrm{Id}-\mu_m\rho\left(\nabla\boldsymbol{u}+(\nabla\boldsymbol{u})^T\right)\right),\Phi_k\right\rangle&=\left\langle-\rho' g\boldsymbol{e_d},\Phi_k\right\rangle,\\ \left\langle(\rho\theta)'_t+\nabla\cdot(\rho\theta\boldsymbol{u}-\mu_h\rho\nabla\theta),\Phi_k\right\rangle&=\langle S_\theta,\Phi_k\rangle\end{aligned}\tag{3.4}$$

and

$$\begin{aligned}\left\langle(\rho q_v)_t+\nabla\cdot\left(\rho q_v\boldsymbol{u}-\mu_q\rho\nabla q_v\right),\Phi_k\right\rangle&=\langle\rho(-C+E),\Phi_k\rangle,\\ \left\langle(\rho q_c)_t+\nabla\cdot\left(\rho q_c\boldsymbol{u}-\mu_q\rho\nabla q_c\right),\Phi_k\right\rangle&=\langle\rho(C-A_1-A_2),\Phi_k\rangle,\\ \left\langle(\rho q_r)_t+\nabla\cdot\left(\rho q_r(-v_q\boldsymbol{e_d}+\boldsymbol{u})-\mu_q\rho\nabla q_r\right),\Phi_k\right\rangle&=\langle\rho(A_1+A_2-E),\Phi_k\rangle,\end{aligned}\tag{3.5}$$

respectively, where $\langle\cdot,\cdot\rangle$ is the weighted scalar product defined in (3.3). Substituting (3.1) and (3.2) into (3.4) and (3.5) and using the orthogonality property (3.3), yield the following deterministic system consisting of $(d+2)(M+1)$ equations for the gPC coefficients of the fluid variables

$$\begin{aligned}
&((\widehat{\rho'})_k)_t+\nabla\cdot(\widehat{\rho\boldsymbol{u}})_k=0,\\
&((\widehat{\rho\boldsymbol{u}})_k)_t+\nabla\cdot\left(\widehat{\mathfrak{N}}_k+(\widehat{p'})_k\mathrm{Id}\right)-\mu_m(\widehat{\boldsymbol{d_1}})_k=-(\widehat{\rho'})_k g\boldsymbol{e_d},\\
&(\widehat{(\rho\theta)'})_k)_t+\nabla\cdot\left(\bar{\theta}(\widehat{\rho\boldsymbol{u}})_k+\widehat{\boldsymbol{\eta}}_k\right)-\mu_h(\widehat{d_2})_k=(\widehat{S_\theta})_k,
\end{aligned}\tag{3.6}$$

and $3(M+1)$ equations for the gPC coefficients of the cloud variables

$$\begin{aligned}
&((\widehat{\rho q_v})_k)_t+\nabla\cdot((\widehat{\boldsymbol{\eta_1^q}})_k)-\mu_q(\widehat{d_1^q})_k=(\widehat{r_1})_k,\\
&((\widehat{\rho q_c})_k)_t+\nabla\cdot((\widehat{\boldsymbol{\eta_2^q}})_k)-\mu_q(\widehat{d_2^q})_k=(\widehat{r_2})_k,\\
&((\widehat{\rho q_r})_k)_t+\nabla\cdot((\widehat{\boldsymbol{\eta_3^q}})_k)-\mu_q(\widehat{d_3^q})_k=(\widehat{r_3})_k,
\end{aligned}\tag{3.7}$$

for $k=0,\dots,M$. The gPC coefficients that appear in (3.6) and (3.7) are defined as follows:

$$\begin{aligned}
&\rho\boldsymbol{u}\otimes\boldsymbol{u}=\sum_{k=0}^{M}\widehat{\mathfrak{N}}_k\Phi_k,\quad p'=\sum_{k=0}^{M}(\widehat{p'})_k\Phi_k,\quad \nabla\cdot\left(\rho\left(\nabla\boldsymbol{u}+(\nabla\boldsymbol{u})^T\right)\right)=\sum_{k=0}^{M}(\widehat{\boldsymbol{d_1}})_k\Phi_k,\\
&\theta'\rho\boldsymbol{u}=\sum_{k=0}^{M}\widehat{\boldsymbol{\eta}}_k\Phi_k,\quad \nabla\cdot(\rho\nabla\theta)=\sum_{k=0}^{M}(\widehat{d_2})_k\Phi_k,\quad S_\theta=\sum_{k=0}^{M}(\widehat{S_\theta})_k\Phi_k,\\
&\rho q_v\boldsymbol{u}=\sum_{k=0}^{M}(\widehat{\boldsymbol{\eta_1^q}})_k\Phi_k,\quad \nabla\cdot(\rho\nabla q_v)=\sum_{k=0}^{M}(\widehat{d_1^q})_k\Phi_k,\quad \rho\,(-C+E)=\sum_{k=0}^{M}(\widehat{r_1})_k\Phi_k,\\
&\rho q_c\boldsymbol{u}=\sum_{k=0}^{M}(\widehat{\boldsymbol{\eta_2^q}})_k\Phi_k,\quad \nabla\cdot(\rho\nabla q_c)=\sum_{k=0}^{M}(\widehat{d_2^q})_k\Phi_k,\quad \rho\,(C-A_1-A_2)=\sum_{k=0}^{M}(\widehat{r_2})_k\Phi_k,\\
&\rho q_r\boldsymbol{u}-\rho q_r v_q\boldsymbol{e_d}=\sum_{k=0}^{M}(\widehat{\boldsymbol{\eta_3^q}})_k\Phi_k,\quad \nabla\cdot(\rho\nabla q_r)=\sum_{k=0}^{M}(\widehat{d_3^q})_k\Phi_k,\quad \rho\,(A_1+A_2-E)=\sum_{k=0}^{M}(\widehat{r_3})_k\Phi_k.
\end{aligned}\tag{3.8}$$

It should be observed that the gPC coefficients in (3.8) arise from the nonlinear terms in (3.4)–(3.5). There exist several approaches for computing these coefficients from the gPC coefficients of the conservative quantities given in (3.1) and (3.2). Due to the complexity of some of the nonlinear terms present in the studied model, we employ a straightforward approach and evaluate the coefficients (3.8) via discrete Legendre/Hermite transform (DT) and inverse discrete Legendre/Hermite transform (IDT). To cite an example, let us consider the $\rho q_v\boldsymbol{u}$ term, for which the gPC coefficients are obtained as follows:

$$\left\{(\widehat{\boldsymbol{\eta_1^q}})_k\right\}_{k=0}^{M}=\mathrm{DT}\left[\frac{\mathrm{IDT}\left[\{(\widehat{\rho q_v})_k\}_{k=0}^{M}\right]\mathrm{IDT}\left[\{(\widehat{\rho\boldsymbol{u}})_k\}_{k=0}^{M}\right]}{\mathrm{IDT}\left[\{(\widehat{\rho'})_k\}_{k=0}^{M}\right]+\bar{\rho}(\boldsymbol{x})}\right],$$

where the DT and IDT operators are defined in (3.11)–(3.13) below. The rest of the gPC coefficients in (3.8) are calculated in a similar way.

- *Discrete transform (DT)* The discrete transform starts with the expansion of a function f in the stochastic space

$$f(\boldsymbol{x},t,\omega)=\sum_{k=0}^{M}\widehat{f}_k(\boldsymbol{x},t)\Phi_k(\omega)\tag{3.9}$$

and by using the orthogonality property (3.3) ends up with the expansion coefficients

$$\widehat{f}_k(\boldsymbol{x},t)=\frac{1}{c_k}\int_\Gamma f(\boldsymbol{x},t,\omega)\Phi_k(\omega)\mu(\omega)\,\mathrm{d}\omega\quad\text{for}\quad 0\le k\le M.\tag{3.10}$$

We approximate the above integral using an appropriate Gaussian quadrature rule. We distinguish between the two cases considered in this paper—Legendre and Hermite polynomials.

(1) For Legendre polynomials $c_k=\frac{1}{2k+1}$, $\Gamma=[-1,1]$, and the expansion coefficients in (3.10) are given by

$$\widehat{f}_k(\boldsymbol{x},t)=\frac{2k+1}{2}\int_{-1}^{1}f(\boldsymbol{x},t,\omega)\Phi_k(\omega)\,\mathrm{d}\omega\quad\text{for}\quad 0\le k\le M.$$

Approximating the above integrals using the Gauss-Legendre quadrature leads to

$$\mathrm{DT}\Big[\{f(\boldsymbol{x},t,\omega_n)\}_{n=0}^N\Big]=\big\{\widehat{f}_k(\boldsymbol{x},t)\big\}_{k=0}^M=\left\{\frac{2k+1}{2}\sum_{n=0}^N\beta_n f(\boldsymbol{x},t,\omega_n)\Phi_k(\omega_n)\right\}_{k=0}^M, \tag{3.11}$$

where ω_n and β_n are the Gauss-Legendre nodes and weights, respectively.

(2) For Hermite polynomials $c_k=k!$, $\Gamma=(-\infty,\infty)$, and the expansion coefficients in (3.10) are given by

$$\widehat{f}_k(\boldsymbol{x},t)=\frac{1}{k!\sqrt{2\pi\sigma_H^2}}\int_{-\infty}^{\infty}f(\boldsymbol{x},t,\omega)\Phi_k(\omega)\boldsymbol{e}^{-\frac{(\omega-\mu_H)^2}{2\sigma_H^2}}\,\mathrm{d}\omega\quad\text{for}\quad 0\le k\le M.$$

Approximating the above integral using the Gauss-Hermite quadrature leads to

$$\mathrm{DT}\Big[\{f(\boldsymbol{x},t,\omega_n)\}_{n=0}^N\Big]=\big\{\widehat{f}_k(\boldsymbol{x},t)\big\}_{k=0}^M=\left\{\frac{1}{k!\sqrt{2\pi\sigma_H^2}}\sum_{n=0}^N\beta_n f(\boldsymbol{x},t,\omega_n)\Phi_k(\omega_n)e^{-\frac{(\omega_n-\mu_H)^2}{2\sigma_H^2}+\omega_n^2}\right\}_{k=0}^M, \tag{3.12}$$

where ω_n and β_n are the Gauss-Hermite nodes and weights, respectively.

- *Inverse discrete transform (IDT)*

The inverse discrete transform maps the expansion coefficients $\{\widehat{f}_k(\boldsymbol{x},t)\}_{k=0}^M$ to the point values $f(\boldsymbol{x},t,\omega_n)$, $0\le n\le N$. To this end we simply compute the point values of f using the gPC expansion (3.9):

$$\mathrm{IDT}\Big[\big\{\widehat{f}_k(\boldsymbol{x},t)\big\}_{k=0}^M\Big]=\big\{f(\boldsymbol{x},t,\omega_n)\big\}_{n=0}^N=\left\{\sum_{k=0}^M\widehat{f}_k(\boldsymbol{x},t)\Phi_k(\omega_n)\right\}_{n=0}^N. \tag{3.13}$$

Remark 3.1. The number of quadrature points N can be chosen equal to the number of expansion coefficients M, or even higher for a more accurate approximation, but, in general, their choice is problem dependent. In the meteorological applications studied in this paper, the choice $N=M$ seems to be rather optimal concerning accuracy vs. computational cost. Recently, adaptive approaches for choosing the number of expansion coefficients have been explored; see, e.g., [14]. Similar techniques can, in principle, be applied to adaptively choosing the number of quadrature points as well.

Remark 3.2. We stress that the quadrature weights β_n and the values $\Phi_k(\omega_n)$, $0\le k\le M$, $0\le n\le N$, which are used in (3.11)–(3.13), can be pre-computed for the code efficiency.

3.2. Discretization of the gPC system

In this section we describe the numerical method used to solve the resulting gPC system (3.6)–(3.7), which we rewrite here in the vector form. To this end, we denote by

$$\widehat{\boldsymbol{w}}:=\Big(\underline{\widehat{\rho'}},\underline{\widehat{\rho\boldsymbol{u}}},\underline{\widehat{(\rho\theta)'}}\Big)^\top,\quad \widehat{\boldsymbol{w}}_q:=\big(\underline{\widehat{\rho q_v}},\underline{\widehat{\rho q_c}},\underline{\widehat{\rho q_r}}\big)^\top\quad\text{and}\quad \widehat{\boldsymbol{W}}:=\big(\widehat{\boldsymbol{w}},\widehat{\boldsymbol{w}}_q\big)^\top$$

the solution vectors of (3.6) and (3.7), respectively. Here, the underline $\underline{(\cdot)}$ denotes the vector of the respective coefficients. For instance, for the solution coefficients we have

$$\underline{\widehat{\rho'}}:=\big((\widehat{\rho'})_0,\ldots,(\widehat{\rho'})_M\big),\quad \underline{\widehat{\rho\boldsymbol{u}}}:=\big((\widehat{\rho u_1})_0,\ldots,(\widehat{\rho u_d})_0;\ldots;(\widehat{\rho u_1})_M,\ldots,(\widehat{\rho u_d})_M\big),$$
$$\underline{\widehat{(\rho\theta)'}}:=\big((\widehat{(\rho\theta)'})_0,\ldots,(\widehat{(\rho\theta)'})_M\big),\quad \underline{\widehat{\rho q_\ell}}=\big((\widehat{\rho q_\ell})_0,\ldots,(\widehat{\rho q_\ell})_M\big),\quad \ell\in\{v,c,r\}.$$

Then, the coupled system can be written as

$$\widehat{\boldsymbol{w}}_t=-\nabla\cdot\boldsymbol{F}(\widehat{\boldsymbol{w}})+\mathfrak{D}(\widehat{\boldsymbol{w}})+\mathfrak{R}(\widehat{\boldsymbol{w}}), \tag{3.14}$$
$$(\widehat{\boldsymbol{w}}_q)_t=-\nabla\cdot\boldsymbol{F}_q(\widehat{\boldsymbol{w}}_q)+\mathfrak{D}_q(\widehat{\boldsymbol{w}}_q)+\mathfrak{R}_q(\widehat{\boldsymbol{w}}_q), \tag{3.15}$$

where $\boldsymbol{F}$ and $\boldsymbol{F}_q$ are convective fluxes and $\mathfrak{D}$, $\mathfrak{R}$ and $\mathfrak{D}_q$, $\mathfrak{R}_q$ denote the diffusion and reaction operators of the respective systems. They are given by

$$\boldsymbol{F}(\widehat{\boldsymbol{w}}):=\Big(\underline{\widehat{\rho\boldsymbol{u}}},\underline{\widehat{p'\mathrm{Id}}}+\underline{\widehat{\mathfrak{N}}},\bar{\theta}\underline{\widehat{\rho\boldsymbol{u}}}+\underline{\widehat{\boldsymbol{\eta}}}\Big)^\top,\quad \mathfrak{D}(\widehat{\boldsymbol{w}}):=\Big(0,\mu_m\underline{\widehat{\boldsymbol{d_1}}},\mu_h\underline{\widehat{d_2}}\Big)^\top,\quad \mathfrak{R}(\widehat{\boldsymbol{w}}):=\Big(0,-\underline{\widehat{\rho'}g\boldsymbol{e_d}},\underline{\widehat{S_\theta}}\Big)^\top, \tag{3.16}$$
$$\boldsymbol{F}_q(\widehat{\boldsymbol{w}}_q):=\Big(\underline{\widehat{\boldsymbol{\eta}_1^q}},\underline{\widehat{\boldsymbol{\eta}_2^q}},\underline{\widehat{\boldsymbol{\eta}_3^q}}\Big)^\top,\quad \mathfrak{D}_q(\widehat{\boldsymbol{w}}_q):=\mu_q\Big(\underline{\widehat{d_1^q}},\underline{\widehat{d_2^q}},\underline{\widehat{d_3^q}}\Big)^\top,\quad \mathfrak{R}_q(\widehat{\boldsymbol{w}}_q):=\big(\underline{\widehat{r_1}},\underline{\widehat{r_2}},\underline{\widehat{r_3}}\big)^\top, \tag{3.17}$$

where the respective components of the above vectors were defined in (3.8). We emphasize that (3.14)–(3.17) is a deterministic system for the gPC expansion coefficients. This system has the same structure as the deterministic system studied in [8]. Therefore, one can directly apply the finite-volume method from [8] for the spatial discretization of the system (3.14)–(3.17) with additional DT and IDT applied for each evaluation of the nonlinear terms on the RHS of (3.14) and (3.15). The expansions (3.8) induce that we first compute the coefficients $\underline{\widehat{\mathfrak{N}}}$, $\underline{\widehat{\boldsymbol{\eta}}}$ and $\underline{\widehat{\boldsymbol{\eta}}}_{\boldsymbol{1}}^{\boldsymbol{q}}$, $\underline{\widehat{\boldsymbol{\eta}}}_{\boldsymbol{2}}^{\boldsymbol{q}}$, $\underline{\widehat{\boldsymbol{\eta}}}_{\boldsymbol{3}}^{\boldsymbol{q}}$ through the transforms and then apply the appropriate approximation of the fluxes as in the deterministic case. For the diffusion terms, we apply the discretization for the respective evaluated functions obtained by IDT and then perform DT to get the diffusion coefficients $\underline{\widehat{\boldsymbol{d}}_{\boldsymbol{1}}}$, $\underline{\widehat{\boldsymbol{d}}_{\boldsymbol{2}}}$ and $\underline{\widehat{\boldsymbol{d}}}_{\boldsymbol{1}}^{\boldsymbol{q}}$, $\underline{\widehat{\boldsymbol{d}}}_{\boldsymbol{2}}^{\boldsymbol{q}}$, $\underline{\widehat{\boldsymbol{d}}}_{\boldsymbol{3}}^{\boldsymbol{q}}$.

The coupling between the atmospheric flow, (3.14), (3.16), and the cloud, (3.15), (3.17), equations is numerically realized by the second-order Strang operator splitting. We evolve the solution from time level t^ν to the next time level $t^{\nu+1} = t^\nu + \Delta t^\nu$, where Δt^ν is the size of the Strang operator splitting time step, in three stages:

$$\widehat{\boldsymbol{W}}(t^{\nu+1}) = \mathcal{S}_{\text{NS}}\left(\frac{\Delta t^\nu}{2}\right)\mathcal{S}_{\text{cloud}}\left(\Delta t^\nu\right)\mathcal{S}_{\text{NS}}\left(\frac{\Delta t^\nu}{2}\right)\widehat{\boldsymbol{W}}(t^\nu), \tag{3.18}$$

where $\mathcal{S}_{\text{NS}}$ and $\mathcal{S}_{\text{cloud}}$ denote numerical solution operators for systems (3.14), (3.16) and (3.15), (3.17), respectively.

For the Navier-Stokes part, we recall that atmospheric flows are weakly compressible and therefore we follow [5,6] and develop an AP finite-volume method, which is capable of accurately and efficiently handling low Mach number regimes. In particular, our AP approach is based on a suitable linear-nonlinear splitting between the stiff and nonstiff parts of the flux:

$$\begin{aligned}
&\boldsymbol{F}(\widehat{\boldsymbol{w}}) = \boldsymbol{F}_L(\widehat{\boldsymbol{w}}) + \boldsymbol{F}_N(\widehat{\boldsymbol{w}}) \quad \text{with} \quad \boldsymbol{F}_L(\widehat{\boldsymbol{w}}) := \left(\underline{\widehat{\rho}\widehat{\boldsymbol{u}}}, \underline{\widehat{p}'\text{ld}}, \bar{\theta}(\underline{\widehat{\rho}\widehat{\boldsymbol{u}}})\right)^\top \text{ and } \boldsymbol{F}_N(\widehat{\boldsymbol{w}}) := \left(0, \underline{\widehat{\mathfrak{N}}}, \underline{\widehat{\boldsymbol{\eta}}}\right)^\top,\\
&\mathfrak{R}(\widehat{\boldsymbol{w}}) = \mathfrak{R}_L(\widehat{\boldsymbol{w}}) + \mathfrak{R}_N(\widehat{\boldsymbol{w}}) \quad \text{with} \quad \mathfrak{R}_L(\widehat{\boldsymbol{w}}) := \left(0, -\underline{\widehat{\rho}' g \boldsymbol{e_d}}, 0\right)^\top \text{ and } \mathfrak{R}_N(\widehat{\boldsymbol{w}}) := \left(0, 0, \underline{\widehat{S_\theta}}\right)^\top,
\end{aligned}$$

and the IMEX AP ARS(2,2,2) method from [4] for time discretization of $\mathcal{S}_{\text{NS}}$ in (3.18). For the latter, we define the stiff linear operator $\mathcal{L} := -\nabla\cdot\boldsymbol{F}_L(\widehat{\boldsymbol{w}}) + \mathfrak{R}_L(\widehat{\boldsymbol{w}})$ and the nonstiff nonlinear operator $\mathcal{N} := -\nabla\cdot\boldsymbol{F}_N(\widehat{\boldsymbol{w}}) + \mathfrak{D}(\widehat{\boldsymbol{w}}) + \mathfrak{R}_N(\widehat{\boldsymbol{w}})$, which are treated implicitly and explicitly, respectively:

$$\begin{aligned}
\widehat{\boldsymbol{w}}\left(t+\frac{\Delta t^\nu}{4}\right) &= \widehat{\boldsymbol{w}}(t) + \frac{\beta\Delta t^\nu}{2}\left[\mathcal{N}\left(\widehat{\boldsymbol{w}}(t)\right) + \mathcal{L}\left(\widehat{\boldsymbol{w}}\left(t+\frac{\Delta t^\nu}{4}\right)\right)\right],\\
\widehat{\boldsymbol{w}}\left(t+\frac{\Delta t^\nu}{2}\right) &= \widehat{\boldsymbol{w}}(t) + \frac{\Delta t^\nu}{2}\left[\left(1-\frac{1}{2\beta}\right)\mathcal{N}\left(\widehat{\boldsymbol{w}}(t)\right) + \frac{1}{2\beta}\mathcal{N}\left(\widehat{\boldsymbol{w}}\left(t+\frac{\Delta t^\nu}{4}\right)\right)\right.\\
&\qquad \left. +(1-\beta)\mathcal{L}\left(\widehat{\boldsymbol{w}}\left(t+\frac{\Delta t^\nu}{4}\right)\right) + \beta\mathcal{L}\left(\widehat{\boldsymbol{w}}\left(t+\frac{\Delta t^\nu}{2}\right)\right)\right],
\end{aligned} \tag{3.19}$$

where $\beta = 1 - 1/\sqrt{2}$.

In (3.19), the nonlinear terms $\mathcal{N}$ are approximated using the Rusanov numerical fluxes, and the second order of accuracy in the nonlinear part is achieved with the help of a piecewise linear reconstruction with the minmod limiter. In the linear terms $\mathcal{L}$, the diffusion operators are discretized using second-order central differences while the reaction operators are directly evaluated using cell averages. This spatial discretization results in a linear system of algebraic equations, which is solved by the restarted GMRES method with ILU preconditioning from the scientific toolkit PETSc (https://petsc.org/).

The cloud equations (3.15), (3.17) are discretized in space by a finite-volume method and in time using an explicit third-order Runge-Kutta method with an enlarged stability region (DUMKA3 from [21,22]).

It should be observed that the microscopic cloud dynamics subsystem has a more severe stability time step restriction than the flow dynamics one and thus the splitting time step Δt^ν in (3.18) is selected based on the following stability restriction for the macroscopic subsystem (3.14), (3.16):

$$\max\left(\frac{\max(\mu_h,\mu_m)}{h^2}, \max_{n=0,\ldots,N}\max_{s=1,\ldots,d}\max_{\boldsymbol{x}\in X}(|u_s(\boldsymbol{x},t^\nu,\omega_n)|)\,\frac{d}{h}\right)\Delta t^\nu < 0.5,$$

where, X is the set of the centers of the finite-volume cells, which for simplicity are assumed to be uniform of size h^d. Then, several small microscopic cloud time evolution steps are to be made within one macroscopic splitting time step through the DUMKA3 method, which chooses microscopic time steps automatically based on the cloud system stiffness coming from the diffusion and reaction terms. The moderate stiffness of the reaction terms comes from power-law-type terms with fractional exponents between -1 and 1. These fractional exponents are present since activation and diffusion processes are modeled explicitly, instead of applying the saturation adjustment.

Remark 3.3. The DUMKA3 method is a third-order Runge-Kutta method, which belongs to the class of explicit Chebyshev-Runge-Kutta methods. Since these methods are explicit, they are more efficient for moderately stiff problems than most of the implicit ODE solvers; see, e.g., [1,15,22]. Additionally, the DUMKA3 method features a low memory demand, adaptive

error control, and an enlarged stability domain along the negative real axis which is still a finite real interval for absolute stability.

4. Numerical experiments

In this section, we present experimental results for the fully random Navier-Stokes-cloud model (2.5), (2.2). In Examples 4.1 and 4.2, we investigate the experimental convergence of our numerical scheme using the well-known meteorological benchmark describing the free convection of a smooth warm and moist air bubble; see, e.g., [7,9]. In Example 4.1, we demonstrate the spatio-temporal convergence as well as the convergence in the stochastic space for the case in which the initial vapor concentration q_v is perturbed by 10% which is realized with a uniform distribution of the randomness. In Example 4.2, we investigate the convergence for the same setup as in Example 4.1 but with normally distributed randomness. Since we use the same numerical method for the space and time discretization as in Example 4.1, in Example 4.2 we just investigate the convergence in the stochastic space. In Examples 4.3 and 4.4, we present the results of the uncertainty study for the Rayleigh-Bénard convection in both 2-D and 3-D. We also compare the results obtained in this work for the fully random model with the deterministic one, in which both the Navier-Stokes equations (2.5) and the cloud equations (2.2) are deterministic, and with the semi-random one, in which the deterministic Navier-Stokes equations are coupled with the random cloud dynamics (this semi-random model was studied in the first part of this work in [8]). We note that the parameters used in the numerical experiments presented below are slightly different from the one used in [8]; however, the main qualitative features remain the same. In both Rayleigh-Bénard experiments (Examples 4.3 and 4.4), we investigate uncertainty propagation, which is triggered by the initial data of the water vapor concentration q_v which we perturbed uniformly. A comparison with a normally distributed initial perturbation or even perturbations of certain parameters is beyond the scope of this work and is left for future study.

In all of the following examples we set $\mu_m = 10^{-3}$ and $\mu_h = \mu_q = 10^{-2}$ in (2.5) and (2.2).

Example 4.1 *(Stochastic initial data with uniformly distributed perturbation).* In this experiment, we simulate free convection of a smooth warm and moist air bubble in 2-D. Due to the shear friction with the surrounding air at the warm/cold air interface, the warm air bubble rises and deforms axisymmetrically and gradually forms a mushroom-like shape. The bubble is placed at $(2500\,\mathrm{m}, 2000\,\mathrm{m})$ in a domain $\Omega = [0,5000]\times[0,5000]\,m^2$. We consider a 10% perturbation of the initial water vapor concentration. This is realized through the following initial conditions in the case of a uniformly distributed randomness for the cloud variables:

$$
\begin{aligned}
&(\widehat{q_v})_0(\boldsymbol{x},0) = 0.005\,\theta'(\boldsymbol{x},0),\quad (\widehat{q_v})_1(\boldsymbol{x},0) = 0.1,\quad (\widehat{q_v})_0(\boldsymbol{x},0),\quad (\widehat{q_v})_k(\boldsymbol{x},0) = 0 \ \text{ for } 2\le k\le M,\\
&(\widehat{q_c})_0(\boldsymbol{x},0) = 10^{-4}\,\theta'(\boldsymbol{x},0),\quad (\widehat{q_c})_k(\boldsymbol{x},0) = 0 \ \text{ for } 1\le k\le M,\\
&(\widehat{q_r})_0(\boldsymbol{x},0) = 10^{-6}\,\theta'(\boldsymbol{x},0),\quad (\widehat{q_r})_k(\boldsymbol{x},0) = 0 \ \text{ for } 1\le k\le M,
\end{aligned}
$$

and for the Navier-Stokes variables:

$$
\begin{aligned}
&(\widehat{\rho'})_0(\boldsymbol{x},0) = -\bar{\rho}(\boldsymbol{x})\frac{(\widehat{\theta'})_0(\boldsymbol{x},0)}{\bar{\theta}(\boldsymbol{x}) + (\widehat{\theta'})_0(\boldsymbol{x},0)},\quad (\widehat{\rho'})_k(\boldsymbol{x},0) = 0 \ \text{ for } 1\le k\le M,\\
&(\widehat{\rho\boldsymbol{u}})_k(\boldsymbol{x},0) = 0 \ \text{ for } 0\le k\le M,\\
&(\widehat{(\rho\theta)'})_0(\boldsymbol{x},0) = \bar{\rho}(\boldsymbol{x})(\widehat{\theta'})_0(\boldsymbol{x},0) + \bar{\theta}(\widehat{\rho'})_0(\boldsymbol{x},0) + (\widehat{\theta'})_0(\boldsymbol{x},0)(\widehat{\rho'})_0(\boldsymbol{x},0),\quad (\widehat{(\rho\theta)'})_k(\boldsymbol{x},0) = 0 \ \text{ for } 1\le k\le M,
\end{aligned}
$$

where

$$
(\widehat{\theta'})_0(\boldsymbol{x},0) = \begin{cases} 2\cos^2\left(\dfrac{\pi r}{2}\right), & r := \sqrt{(x_1-2500)^2+(x_2-2000)^2}\le 2000,\\ 0, & \text{otherwise,}\end{cases}\qquad (\widehat{\theta'})_k(\boldsymbol{x},0) = 0 \ \text{ for } 1\le k\le M.
$$

Additionally, we set $\bar{\theta} = 285\,\mathrm{K}$, $p_0 = \bar{p} = 10^5\,\mathrm{Pa}$ and

$$
\bar{\rho}(\boldsymbol{x}) = \frac{p_0}{R\bar{\theta}(\boldsymbol{x})}\left(1 - \frac{g x_2}{c_p\bar{\theta}}\right)^{\frac{1}{\gamma-1}}
$$

with $c_p = 1005\,\mathrm{J/(kg\cdot K)}$, $c_v = 718\,\mathrm{J/(kg\cdot K)}$ and $\gamma = c_p/c_v$. We start here with nonzero values for the cloud drops concentration q_c and the rain concentration q_r to avoid values close to the machine precision since the main purpose of the test is the convergence study. Furthermore, we apply the no-slip boundary conditions for the velocities and homogeneous Neumann boundary conditions for the remaining variables, that is, $\nabla\rho'\cdot\boldsymbol{n} = 0$, $\nabla(\rho\theta)'\cdot\boldsymbol{n} = 0$ and $\nabla(\rho q_\ell)\cdot\boldsymbol{n} = 0$, $\ell\in\{v,c,r\}$.

In Fig. 1, we depict the expected values of the potential temperature θ and the cloud variables q_v, q_c and q_r, computed using a 160×160 uniform mesh at time 200s with $M = L = 3$. For comparison purposes, in Fig. 2 we show the potential temperature θ and the water vapor concentration q_v computed using the deterministic Navier-Stokes-cloud model and the

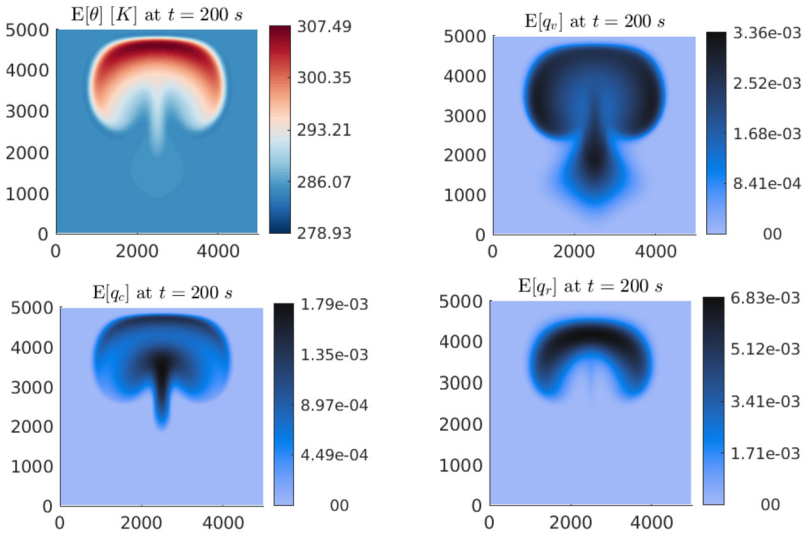

Fig. 1. Example 4.1: The expected values of the potential temperature θ, the water vapor concentration q_v, cloud drops concentration q_c and rain concentration q_r computed using the fully random model.

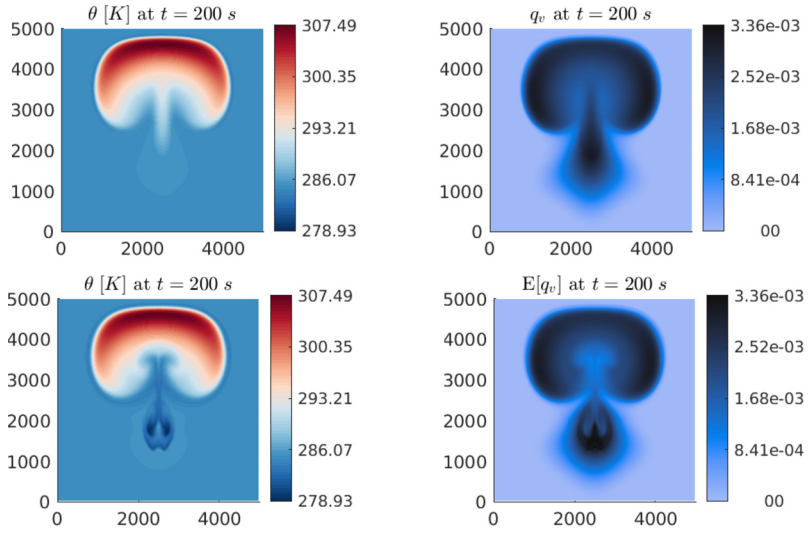

Fig. 2. Example 4.1: The potential temperature θ and the water vapor concentration q_v computed using the deterministic model (first row) and the potential temperature θ and the expected values of the water vapor concentration q_v computed using the semi-random model (second row).

potential temperature θ and the expected values of the water vapor concentration q_v computed using the semi-random Navier-Stokes-cloud model. Note that for a better comparison, we have used the same vertical scales for presenting the results in Figs. 1 and 2. It can be observed that the fully random results are more smeared compared to the deterministic ones and that in the fully random experiment no additional vortices beneath the bubble have been developed and the results are slight variations of the deterministic ones, which is to be expected. In order to investigate the appearance of the vortices in the semi-random case (see the second row Fig. 2), we depict in Fig. 3 the semi-random results obtained for the smaller initial water vapor perturbation taken as 1%, 5% and 7%. One can clearly see, the vortices develop gradually with higher perturbation and that the 1% perturbation results are very close to the deterministic ones. Thus, the vortex features of the solutions obtained with the semi-random model seem to result from the missing feedback to the dynamics of the fluid and are not a defect of the numerical method. We also note that in the semi-random model, the energy conservation is (slightly) violated. This might lead to the differences in the simulations, since the dynamics is then driven by the averaged latent heat release and not by the one in the realization.

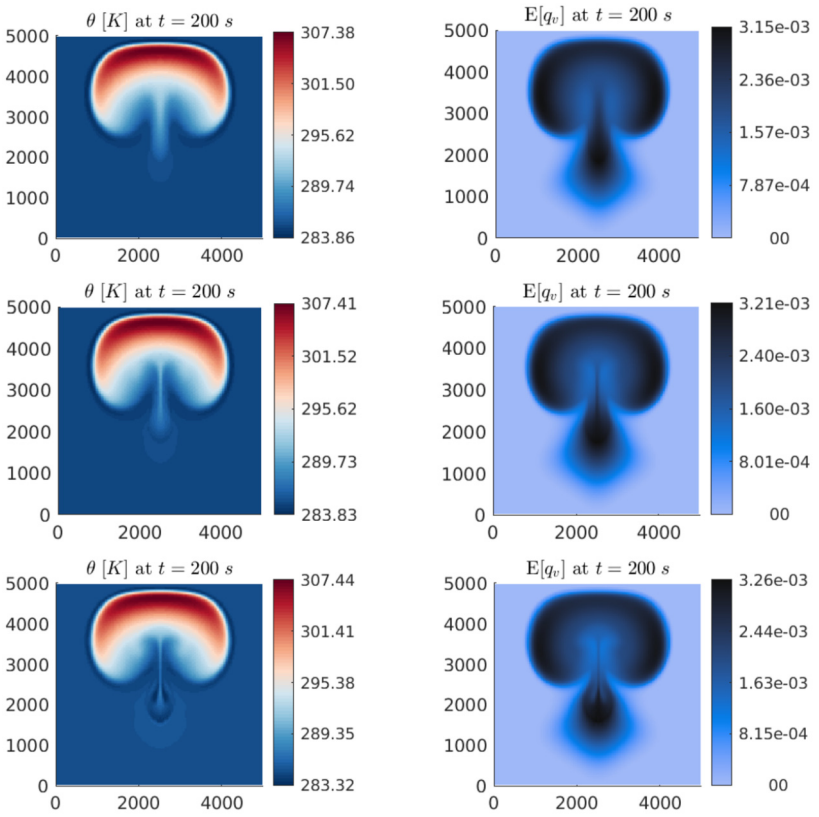

Fig. 3. Example 4.1: The potential temperature θ (left column) and the expected value of the water vapor concentration q_v (right column) computed using the semi-random model for 1% (first row), 5% (second row) and 7% (third row) of initial water vapor perturbations.

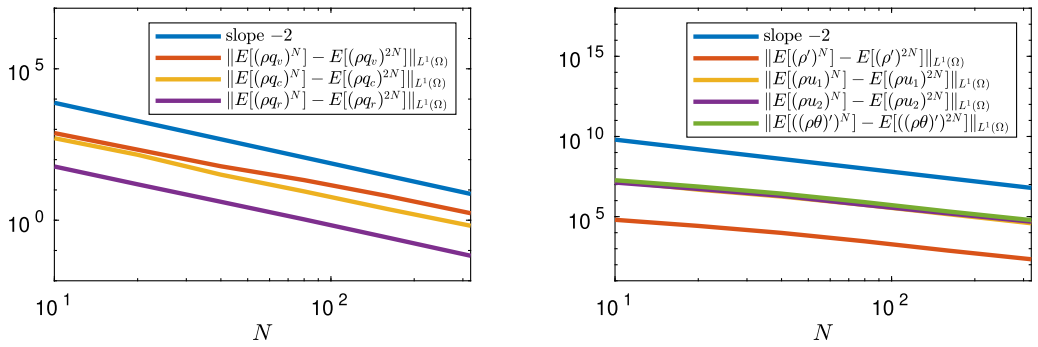

Fig. 4. Example 4.1: Spatio-temporal L^1 convergence study for the expected values of the cloud variables q_v q_c and q_r (left) and the flow variables ρ', ρu_1, ρu_2 and $(\rho\theta)'$ (right) computed at time $t = 10s$ using the fully random model with the constant time step $\Delta t = {}^{256}/_{100N}$.

In Fig. 4, we present the spatio-temporal convergence study for the expected values of the cloud and flow variables at the time $t = 10s$. We compute the solutions on different $N \times N$ uniform meshes with $M = L = 3$. As in the deterministic case presented in [8], one can clearly see a second-order convergence for the studied fully random model.

The stochastic convergence studies are presented in Figs. 5 and 6 for the cloud and Navier-Stokes variables, respectively, at time $t = 10s$ using a 160×160 uniform mesh. We compute the difference between the approximate solutions with different numbers of modes M and $L = M$ and the reference solution obtained with 20 stochastic modes and $L = 19$. One can observe a spectral convergence with an approximate rate of $e^{-0.3M}$. One can also see that the error of the rain drops in Fig. 6 (right) basically stays constant at some point because in this case it approaches the machine precision.

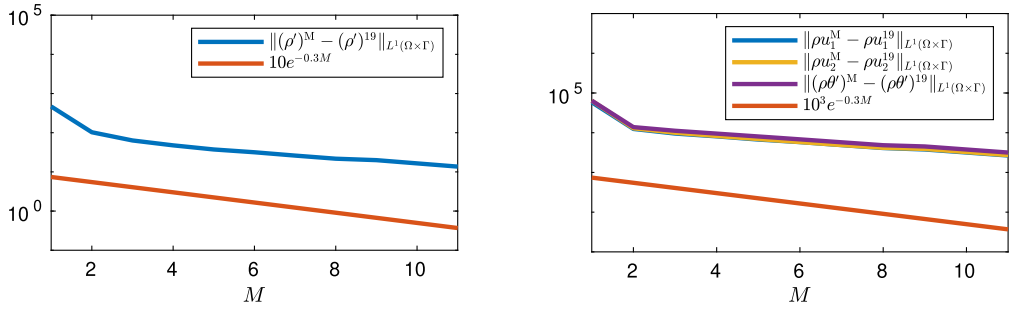

Fig. 5. Example 4.1: L^1 convergence study for the Navier-Stokes variables ρ' (left) and ρu_1, ρu_2 and $(\rho\theta)'$ (right) in the stochastic space computed at time $t = 10s$ using the fully random model with the constant time step $\Delta t = 0.01$.

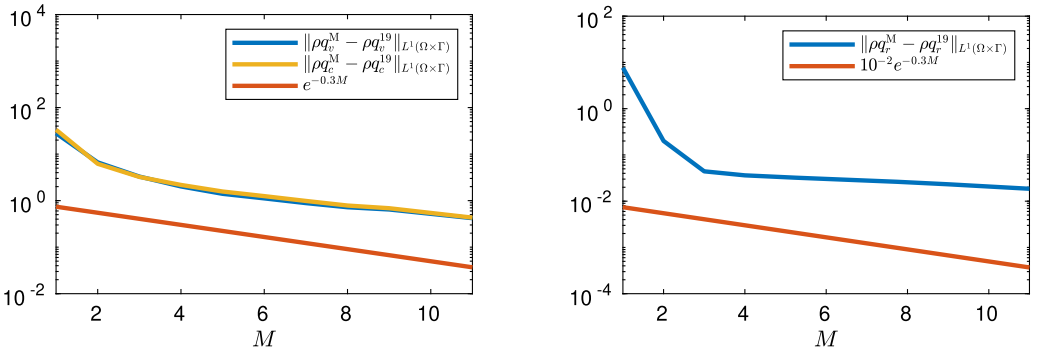

Fig. 6. Example 4.1: L^1 convergence study for the cloud variables ρq_v and q_c (left) and q_r (right) in the stochastic space computed at time $t = 10s$ using the fully random model with the constant time step $\Delta t = 0.01$.

Example 4.2 *(Stochastic initial data with normally distributed perturbation).* In this experiment, we demonstrate that the convergence of the stochastic Galerkin method for the fully stochastic model does not depend on the choice of the distribution of the randomness. For this purpose, we choose the same initial conditions as in Example 4.1, but this time with a normally $\mathcal{N}(0, 1)$ distributed perturbation.

In Fig. 7, we compare the solutions (the potential temperature θ and the water vapor concentration q_v) computed using the deterministic, semi-random and fully random Navier-Stokes-cloud models. For a better comparison, we have used the same vertical scales for presenting the results. As in the previous example, one can observe that in the fully random experiment no additional vortices beneath the bubble have been developed and the results are slight variations of the deterministic ones. Thus, the vortex features of the semi-random results are independent of the distributions of the initial perturbation and caused by the missing feedback to the dynamics of the fluid.

Next, we investigate the influence of the choice of distribution for the initial perturbation. In Fig. 8, we depict the cloud drops concentration q_c computed using the fully random model with the initial normally and uniformly distributed perturbations; the latter one was computed in Example 4.1. For a better comparison, we have used the same vertical scales for presenting the results. Since the initial perturbation is rather small, the results look very alike. In general, both simulations smear the boundaries of the bubble. However, the smearing with the normal distribution is not as strong as with the uniform distribution. This effect is due to the concentrated shape of the normal distribution around the expected value; thus, the different realizations are closer to the averaged potential temperature as a feedback to the energy equation.

The convergence studies in the stochastic space are presented in Figs. 9 and 10 for the cloud and Navier-Stokes variables, respectively, at time $t = 10s$ using a 160×160 uniform mesh. We computed the difference between the approximate solutions with different numbers of modes M and $L = M$ and the reference solution obtained with 12 stochastic modes and $L = 11$. As in the case with a uniform distribution studied in Example 4.1, one can observe a spectral convergence with an approximate rate of $e^{-0.3M}$. This demonstrates that the experimental convergence rate is independent of the chosen distribution.

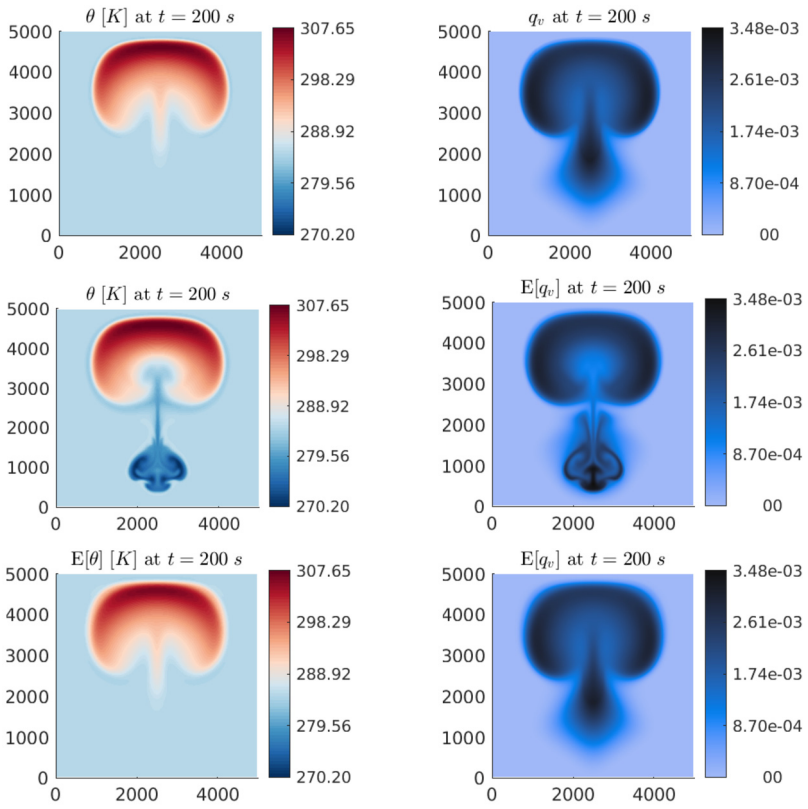

Fig. 7. Example 4.2: The potential temperature θ and the water vapor concentration q_v computed using the deterministic model (first row); the potential temperature θ and the expected values of the water vapor concentration q_v computed using the semi-random model (second row); the expected values of the potential temperature θ and the water vapor concentration q_v computed using the fully random model (third row).

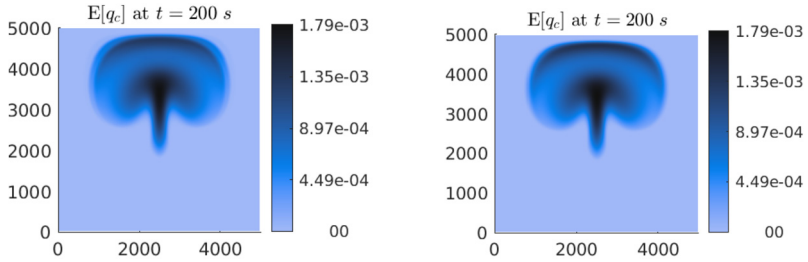

Fig. 8. Examples 4.1 and 4.2: The expected values of the cloud drops concentration q_c computed using the fully random model with the initial normally (left) and uniformly (right) distributed perturbations.

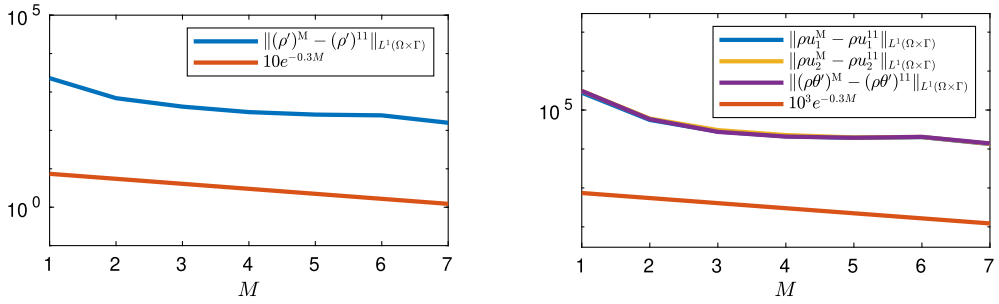

Fig. 9. Example 4.2: L^1 convergence study for the Navier-Stokes variables ρ' (left) and ρu_1, ρu_2 and $(\rho\theta)'$ (right) in the stochastic space computed at time $t = 10s$ using the fully random model with the constant time step $\Delta t = 0.01$.

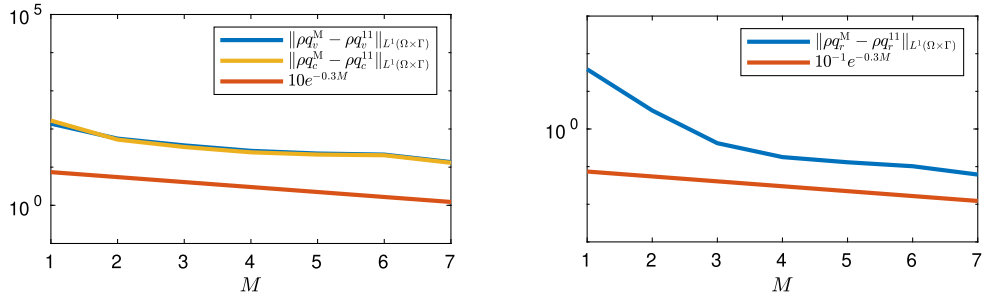

Fig. 10. Example 4.2: L^1 convergence study for the cloud variables ρq_v and q_c (left) and q_r (right) in the stochastic space computed at time $t = 10s$ using the fully random model with the constant time step $\Delta t = 0.01$.

Example 4.3 *(Rayleigh-Bénard convection in 2-D).* We consider a 2-D stochastic Rayleigh-Bénard convection simulated on a domain $\Omega = [0, 5000] \times [0, 1000]\,m^2$ that has been discretized using a uniform 160×160 mesh. The initial data for the cloud variables are

$$(\widehat{q_v})_0(\boldsymbol{x}, 0) = 0.025(\theta'(\boldsymbol{x}, 0))_+, \quad (\widehat{q_v})_1(\boldsymbol{x}, 0) = 0.1(\widehat{q_v})_0(\boldsymbol{x}, 0), \quad (\widehat{q_v})_k(\boldsymbol{x}, 0) = 0 \text{ for } 2 \le k \le M,$$
$$(\widehat{q_c})_0(\boldsymbol{x}, 0) = 10^{-4}(\theta'(\boldsymbol{x}, 0))_+, \quad (\widehat{q_c})_k(\boldsymbol{x}, 0) = 0 \text{ for } 1 \le k \le M,$$
$$(\widehat{q_r})_0(\boldsymbol{x}, 0) = 10^{-6}(\theta'(\boldsymbol{x}, 0))_+, \quad (\widehat{q_r})_k(\boldsymbol{x}, 0) = 0 \text{ for } 1 \le k \le M,$$

and for the Navier-Stokes variables are

$$(\widehat{\rho'})_0(\boldsymbol{x}, 0) = -\bar{\rho}(\boldsymbol{x})\frac{(\widehat{\theta'})_0(\boldsymbol{x}, 0)}{\bar{\theta}(\boldsymbol{x}) + (\widehat{\theta'})_0(\boldsymbol{x}, 0)}, \quad (\widehat{\rho'})_k(\boldsymbol{x}, 0) = 0 \text{ for } 1 \le k \le M,$$
$$(\widehat{\rho u_1})_0(\boldsymbol{x}, 0) = 0.001\big[(\widehat{\rho'})_0(\boldsymbol{x}, 0) + \bar{\rho}(\boldsymbol{x})\big], \quad (\widehat{\rho u_1})_k(\boldsymbol{x}, 0) = 0 \text{ for } 1 \le k \le M,$$
$$(\widehat{\rho u_2})_0(\boldsymbol{x}, 0) = \sin\left(\frac{\pi x_2}{500}\right)\big[(\widehat{\rho'})_0(\boldsymbol{x}, 0) + \bar{\rho}(\boldsymbol{x})\big], \quad (\widehat{\rho u_2})_k(\boldsymbol{x}, 0) = 0 \text{ for } 1 \le k \le M,$$
$$(\widehat{(\rho\theta)'})_0(\boldsymbol{x}, 0) = \bar{\rho}(\boldsymbol{x})(\widehat{\theta'})_0(\boldsymbol{x}, 0) + \bar{\theta}(\widehat{\rho'})_0(\boldsymbol{x}, 0) + (\widehat{\theta'})_0(\boldsymbol{x}, 0)(\widehat{\rho'})_0(\boldsymbol{x}, 0), \quad (\widehat{(\rho\theta)'})_k(\boldsymbol{x}, 0) = 0 \text{ for } 1 \le k \le M,$$

where

$$\begin{aligned}
&(\widehat{\theta'})_0(\boldsymbol{x}, 0) = 0.6\sin\left(\frac{\pi x_2}{500}\right), \quad (\widehat{\theta'})_k(\boldsymbol{x}, 0) = 0 \text{ for } 1 \le k \le M,\\
&\bar{\theta}(\boldsymbol{x}) = 284 - \frac{x_2}{1000}, \quad \bar{\rho}(\boldsymbol{x}) = \frac{p_0}{R\bar{\theta}(\boldsymbol{x})}\pi_e(\boldsymbol{x})^{\frac{1}{\gamma-1}}, \quad \pi_e(\boldsymbol{x}) = 1 - \frac{g x_2}{c_p\bar{\theta}(\boldsymbol{x})}.
\end{aligned} \tag{4.1}$$

We implement the following Dirichlet boundary conditions for the potential temperature:

$$\theta(x_2 = 0) = 284\,\mathrm{K} \quad \text{and} \quad \theta(x_2 = 1000) = 283\,\mathrm{K},$$

as well as the periodic boundary conditions for all of the variables in the horizontal direction, no-slip boundary conditions for the velocities at the vertical boundaries, and zero Neumann conditions for the remaining variables in the vertical direction, that is, $\nabla\rho' \cdot \boldsymbol{n} = 0$. Also, these boundary conditions have to be projected onto the stochastic space. The projections of the periodic, no-slip and Neumann boundary conditions are straightforward and lead to the same conditions as in the deterministic case for all of the expansion coefficients of the respective variable. Here, we briefly explain how the projection of the Dirichlet boundary conditions works. We implement the Dirichlet boundary conditions for the potential temperature using $\rho\theta(\boldsymbol{x}, t, \omega) = (\rho\theta)'(\boldsymbol{x}, t, \omega) + \overline{\rho\theta}(\boldsymbol{x})$. Rearranging and inserting the expansion for $\rho'(\boldsymbol{x}, t, \omega)$ and $(\rho\theta)'(\boldsymbol{x}, t, \omega)$ gives

$$\begin{aligned}
&(\rho\theta)'(\boldsymbol{x}, t, \omega) - \rho'(\boldsymbol{x}, t, \omega)\theta(\boldsymbol{x}, t, \omega) = \bar{\rho}(\boldsymbol{x})\theta(\boldsymbol{x}, t, \omega) - \overline{\rho\theta}(\boldsymbol{x})\\
\Longleftrightarrow\ &\sum_{k=0}^{M}(\widehat{(\rho\theta)'})_k(\boldsymbol{x}, t)\Phi_k(\omega) - \left(\sum_{k=0}^{M}(\widehat{\rho'})_k(\boldsymbol{x}, t)\Phi_k(\omega)\right)\theta(\boldsymbol{x}, t, \omega) = \bar{\rho}(\boldsymbol{x})\theta(\boldsymbol{x}, t, \omega) - \overline{\rho\theta}(\boldsymbol{x}).
\end{aligned}$$

At θ is constant at the boundary, applying the projection leads to

$$(\widehat{(\rho\theta)'})_0(x_2 = 0, t) - (\widehat{\rho'})_0(x_2 = 0, t)\theta(x_2 = 0) = \bar{\rho}(x_2 = 0)\theta(x_2 = 0) - \overline{\rho\theta}(x_2 = 0),$$
$$(\widehat{(\rho\theta)'})_k(x_2 = 0, t) - (\widehat{\rho'})_k(x_2 = 0, t)\theta(x_2 = 0) = 0 \text{ for } 1 \le k \le M,$$

and analogously for $x_2 = 1000$.

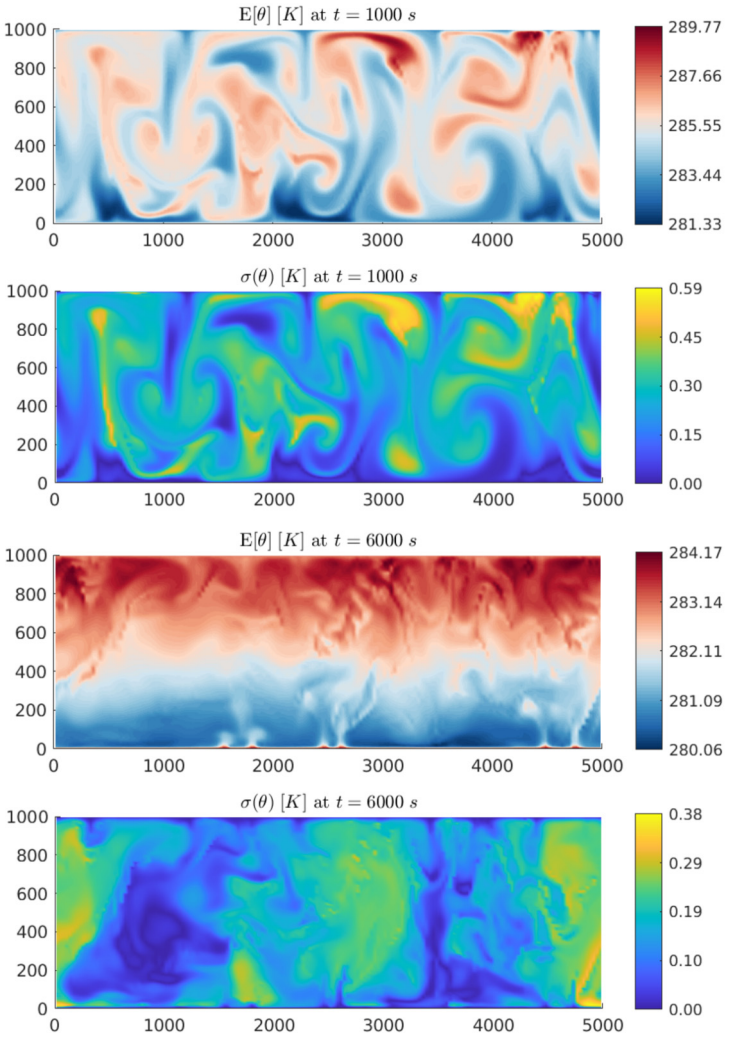

Fig. 11. Example 4.3: Expected value and standard deviation of the potential temperature θ at $t = 1000s$ and $6000s$.

In Figs. 11 and 12, we present snapshots of the expected values and standard deviations of the potential temperature and the cloud variables at times $t = 1000$ and $6000s$, respectively. Additionally, in Fig. 13, we plot the differences between the expected value of the water vapor concentration and the saturation mixing ratio $E[q_v] - q_*$ at the same times. As one can observe, the potential temperature exhibits a strong vertical gradient at time $t = 1000s$. Similarly to the deterministic and semi-random cases, at a later time $t = 6000s$, supersaturated regions are formed in the rolls where the convection takes place leading to the overall roll-like cloud flow structure.

In Figs. 14 and 15, we present the time evolution of the mean expected value per m^2 as well as the mean standard deviation per m^2 for the potential temperature and the cloud variables. In d space dimensions these quantities can be computed for uniformly distributed perturbations in the following way:

$$\mathbb{E}\left[\frac{h^d}{|\Omega|}\sum_{i=1}^{N^d}(q_\ell)_i\right] = \frac{h^d}{|\Omega|}\sum_{i=1}^{N^d}\mathbb{E}\left[(q_\ell)_i\right] = \frac{h^d}{|\Omega|}\sum_{i=1}^{N^d}((\widehat{q_\ell})_0)_i, \quad \sigma\left(\frac{h^d}{|\Omega|}\sum_{i=1}^{N^d}(q_\ell)_i\right) = \frac{h^d}{|\Omega|}\sqrt{\sum_{k=1}^{M}\frac{1}{2k+1}\left(\sum_{i=1}^{N^d}((\widehat{q_\ell})_k)_i\right)^2},$$

where N^d is the number of mesh cells and $\ell \in \{v, c, r\}$. We compare the solutions using 0% (purely deterministic model) and 10% of perturbation of the initial data in q_v, where for 10% of perturbation the solutions are added in both fully- and semi-random Navier-Stokes-cloud models. The time evolution of the averaged quantities clearly shows the differences between the semi-random and fully random models. In all shown cases (including the purely deterministic one), the time evolution starts with cloud formation and thus increase of cloud water on the expense of water vapor and also latent heat release (increase of θ). However, for the semi-random model the rain formation starts earlier than in the deterministic and fully random simulations. Since rain is falling into subsaturated regions which induces evaporation, this leads to a different time

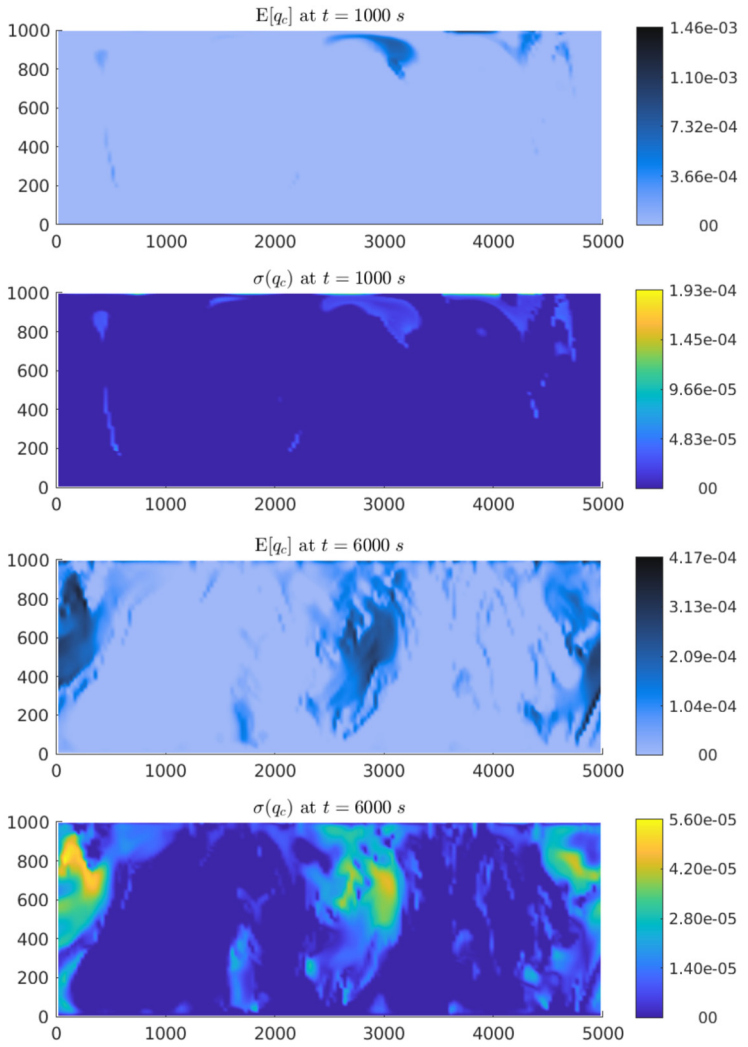

Fig. 12. Example 4.3: Expected value and standard deviation of the cloud drops concentration q_c at $t = 1000s$ and $6000s$.

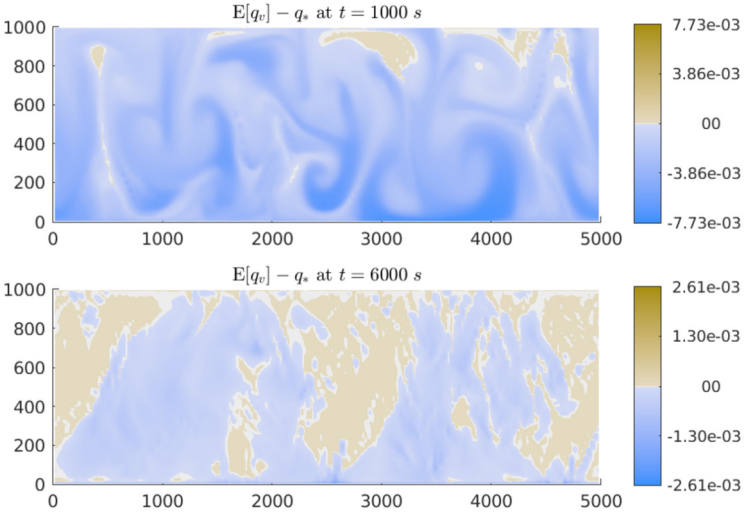

Fig. 13. Example 4.3: Difference between the expected value of the water vapor concentration and the saturation mixing ratio ($\mathbb{E}[q_v] - q_*$) at $t = 1000s$ and $6000s$.

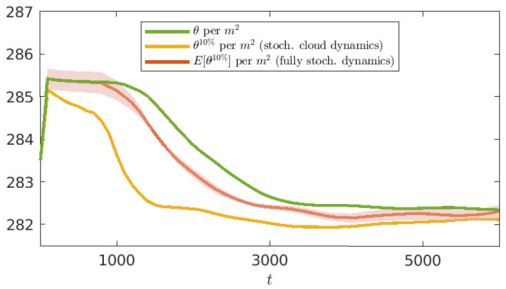

Fig. 14. Example 4.3: Time evolution of the expected values with their standard deviations (shaded region) for the potential temperature θ per m^2 using 0% (purely deterministic case) and 10% perturbation of the initial data in q_v, where the latter was simulated using both fully- and semi-random models.

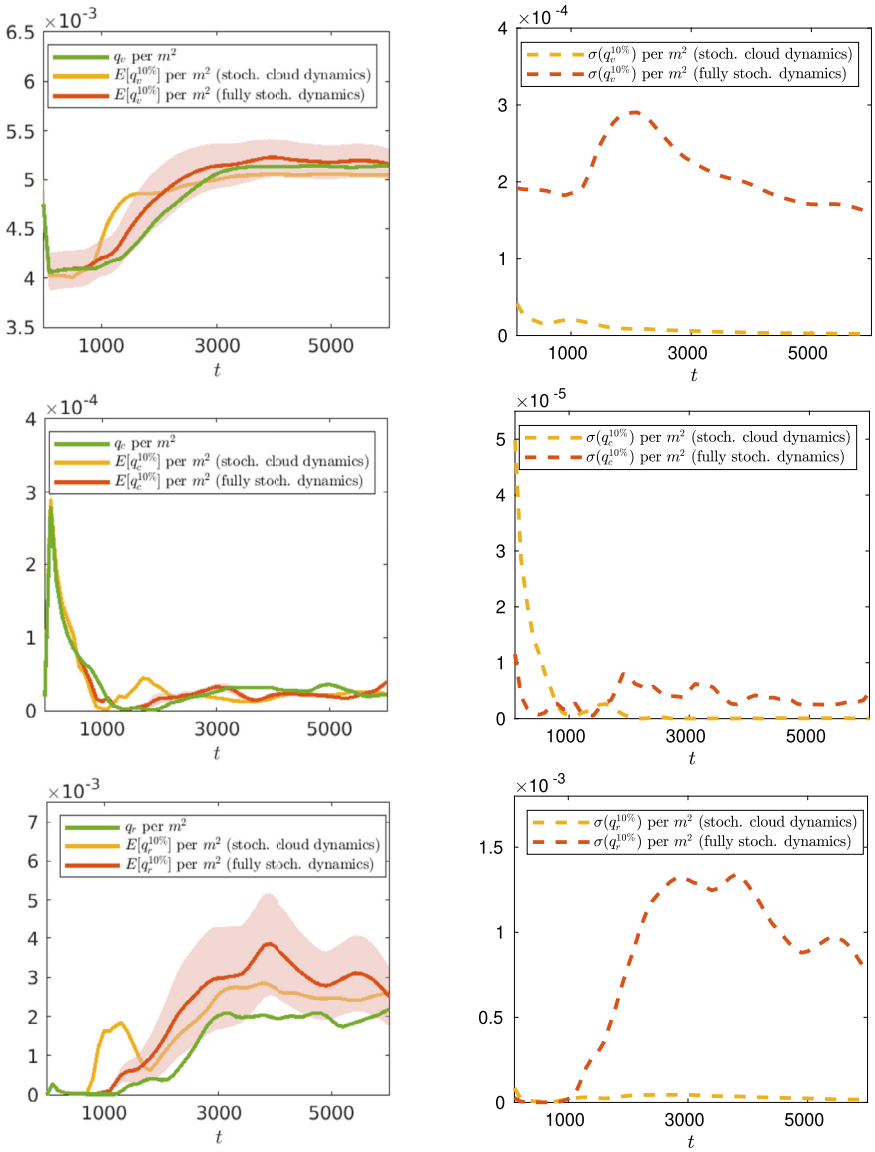

Fig. 15. Example 4.3: Time evolution of the expected values with their standard deviations for the cloud variables per m^2 (shaded region, left column) and standard deviation (right column) using 0% (purely deterministic case) and 10% perturbation of the initial data in q_v, where the latter was simulated using both fully- and semi-random models.

evolution in all variables. Generally, we observe a much stronger cooling effect of the system due to evaporation of rain in the semi-random model than in the other simulations. This is probably due to the use of the expected values of the terms for phase changes in the energy equation. Although the general qualitative behavior in the time evolution of the expected values is quite similar, the absolute values differ quite substantially. The same is true for the standard deviations of the cloud variables q_v q_c and q_r as shown in the right column of Fig. 15; the variation in the water variables (and also in θ) is much larger for the fully random model than for the semi-random one. This is also reasonable, since the fully random model can capture the correct feedback of the latent heat release in the phase changes for the "different realizations", whereas the semi-random model only feeds back the averaged potential temperature, leading to a smaller variability. Some examples of the expected values and the related standard deviations for θ, q_c and the super/subsaturation (in terms of $\mathbb{E}[q_v] - q_*$) are shown in Figs. 11–13.

Example 4.4 *(Rayleigh-Bénard convection in 3-D).* In the final example, we consider a 3-D stochastic Rayleigh-Bénard convection. The initial data for the cloud variables are

$$(\widehat{q_v})_0(\boldsymbol{x},0) = 0.025(\theta'(\boldsymbol{x},0))_+, \quad (\widehat{q_v})_1(\boldsymbol{x},0) = \nu(\widehat{q_v})_0(\boldsymbol{x},0), \quad (\widehat{q_v})_k(\boldsymbol{x},0) = 0 \text{ for } 2 \le k \le M,$$
$$(\widehat{q_c})_0(\boldsymbol{x},0) = 10^{-4}(\theta'(\boldsymbol{x},0))_+, \quad (\widehat{q_c})_k(\boldsymbol{x},0) = 0 \text{ for } 1 \le k \le M,$$
$$(\widehat{q_r})_0(\boldsymbol{x},0) = 10^{-6}(\theta'(\boldsymbol{x},0))_+, \quad (\widehat{q_r})_k(\boldsymbol{x},0) = 0 \text{ for } 1 \le k \le M,$$

with $\nu = 0$, 0.1, 0.2 or 0.5, which correspond to 0% (pure deterministic case), 10%, 20% or 50% perturbation of the initial water vapor concentration. For the Navier-Stokes variables we take purely deterministic initial data, which in terms of their expansion coefficients read as

$$(\widehat{\rho'})_0(\boldsymbol{x},0) = -\bar{\rho}(\boldsymbol{x})\frac{(\widehat{\theta'})_0(\boldsymbol{x},0)}{\bar{\theta}(\boldsymbol{x}) + (\widehat{\theta'})_0(\boldsymbol{x},0)}, \quad (\widehat{\rho u_1})_0(\boldsymbol{x},0) = 0.001\big[(\widehat{\rho'})_0(\boldsymbol{x},0) + \bar{\rho}(\boldsymbol{x})\big],$$
$$(\widehat{\rho u_2})_0(\boldsymbol{x},0) = 0.001\big[(\widehat{\rho'})_0(\boldsymbol{x},0) + \bar{\rho}(\boldsymbol{x})\big], \quad (\widehat{\rho u_3})_0(\boldsymbol{x},0) = \sin\Big(\frac{\pi x_3}{500}\Big)\big[(\widehat{\rho'})_0(\boldsymbol{x},0) + \bar{\rho}(\boldsymbol{x})\big],$$
$$(\widehat{(\rho\theta)'})_0(\boldsymbol{x},0) = \bar{\rho}(\boldsymbol{x})(\widehat{\theta'})_0(\boldsymbol{x},0) + \bar{\theta}(\widehat{\rho'})_0(\boldsymbol{x},0) + (\widehat{\theta'})_0(\boldsymbol{x},0)(\widehat{\rho'})_0(\boldsymbol{x},0),$$
$$(\widehat{\rho'})_k(\boldsymbol{x},0) = (\widehat{\rho u_1})_k(\boldsymbol{x},0) = (\widehat{\rho u_2})_k(\boldsymbol{x},0) = (\widehat{\rho u_3})_k(\boldsymbol{x},0) = (\widehat{(\rho\theta)'})_k(\boldsymbol{x},0) = 0 \text{ for } 1 \le k \le M,$$

where

$$(\widehat{\theta'})_0(\boldsymbol{x},0) = 0.6\sin\Big(\frac{\pi x_3}{500}\Big),$$

and $\bar{\theta}(\boldsymbol{x})$ and $\bar{\rho}(\boldsymbol{x})$ are chosen as in (4.1). The solution is computed in the domain $\Omega = [0,5000]\times[0,5000]\times[0,1000]\,m^3$ which is discretized using a uniform $50\times50\times50$ mesh.

In Figs. 16–18, we present the influence of the 10%, 20% and 50% initial water vapor perturbation on the expected values of the potential temperature, cloud droplets and rain drops concentration at times $t = 1000s$ and $6000s$. The influence on the supersaturated and subsaturated regions is highlighted as a 2-D slice along $x_1 = 3000$ in Fig. 19, where we depict the difference between the expected water vapor concentration and the saturation mixing ratio. For a better comparison, we have used the same vertical scales in all of the plots. Here, one can clearly observe a different behavior compared with the semi-random case. The vertical gradient of the potential temperature increases as the size of the initial perturbations increases (see Fig. 16), while the pattern of the developed convection cells is similar for different perturbations. The latent heat release increases the vertical motions in the convective cells, which leads to additional feedback, such as stronger and more cloud formation (see Fig. 17), which in turn leads to the formation of a much larger amount of rain water, especially at a later time $t = 6000s$ (see Fig. 18). At the time $t = 1000s$ one can see that the roll-like structure of the clouds in the deterministic case (that is, with 0% perturbation) again end up in a more cell-like structure in the initially perturbed cases.

In Figs. 20 and 21, we show the time evolution of the mean expected value per m^3 as well as the mean standard deviation per m^3 for the potential temperature and cloud variables in the cases with 0% (purely deterministic), 10%, 20% and 50% perturbation of the initial water vapor concentration. For increasing perturbations, the spread is increased, mostly for the water vapor concentration q_v and the rain concentration q_r. The averaged quantities are dominated by the positive perturbations, leading to (i) earlier cloud formation, (ii) thicker clouds due to more available water vapor, and (iii) enhanced rain formation. These three features can be clearly seen in the case of the largest initial perturbation (50%), where a large spread in water vapor concentration is accompanied by a strong increase in cloud water and an earlier onset of strong precipitation. Due to the strong rain formation the cloud concentration decreases when the perturbation size increases and also the amount of supersaturated regions is much smaller as can be observed in Fig. 19 which leads to less new formation of clouds. We would also like to note that the spread is only given by the standard deviation, whereas the actual minima (for instance, almost no cloud formation) cannot be seen directly, although these scenarios are possible. Overall, one can see that the time evolution for the deterministic simulation as well as for perturbations with 10% and 20% behave quite similarly and the averaged quantities follow closely the same evolution, although the standard deviations increase quite substantially. However, for larger perturbations (50%), the time evolution of the expected values of q_c and q_r is strongly disturbed and shows large deviations from the other simulations. This can also be seen in the 3-D panels at the later time $t = 6000s$.

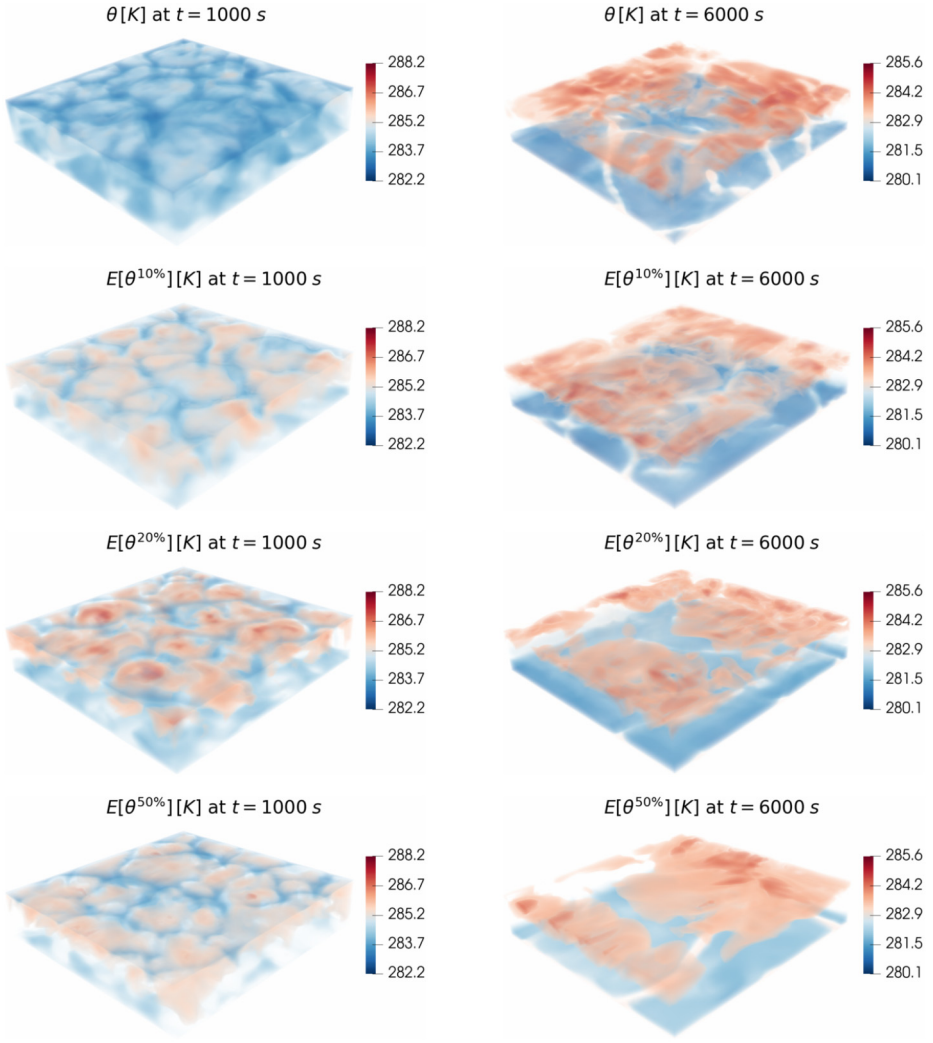

Fig. 16. Example 4.4: Expected value of the potential temperature θ at times $t = 1000s$ and $6000s$ with 0%, 10%, 20% and 50% perturbations of the initial water vapor concentration.

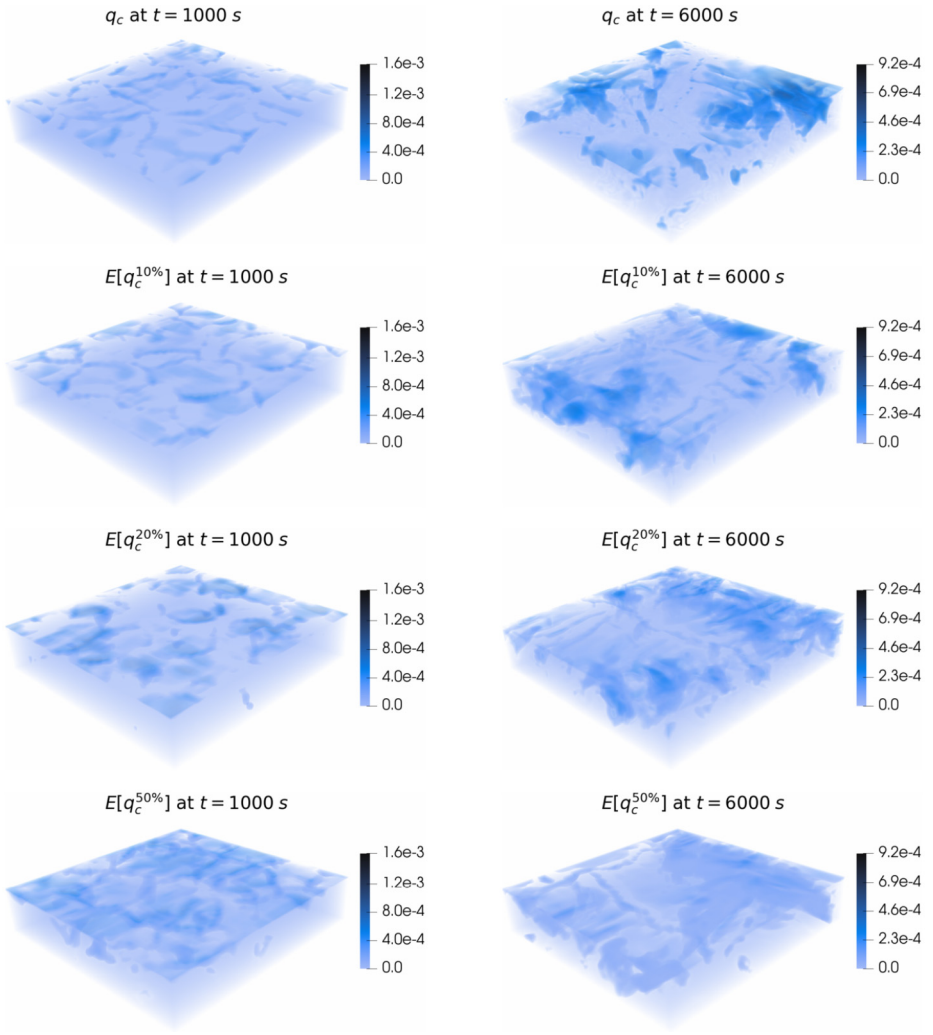

Fig. 17. Example 4.4: Expected value of the cloud drops concentration q_c at times $t = 1000s$ and $6000s$ with 0%, 10%, 20% and 50% perturbations of the initial water vapor concentration.

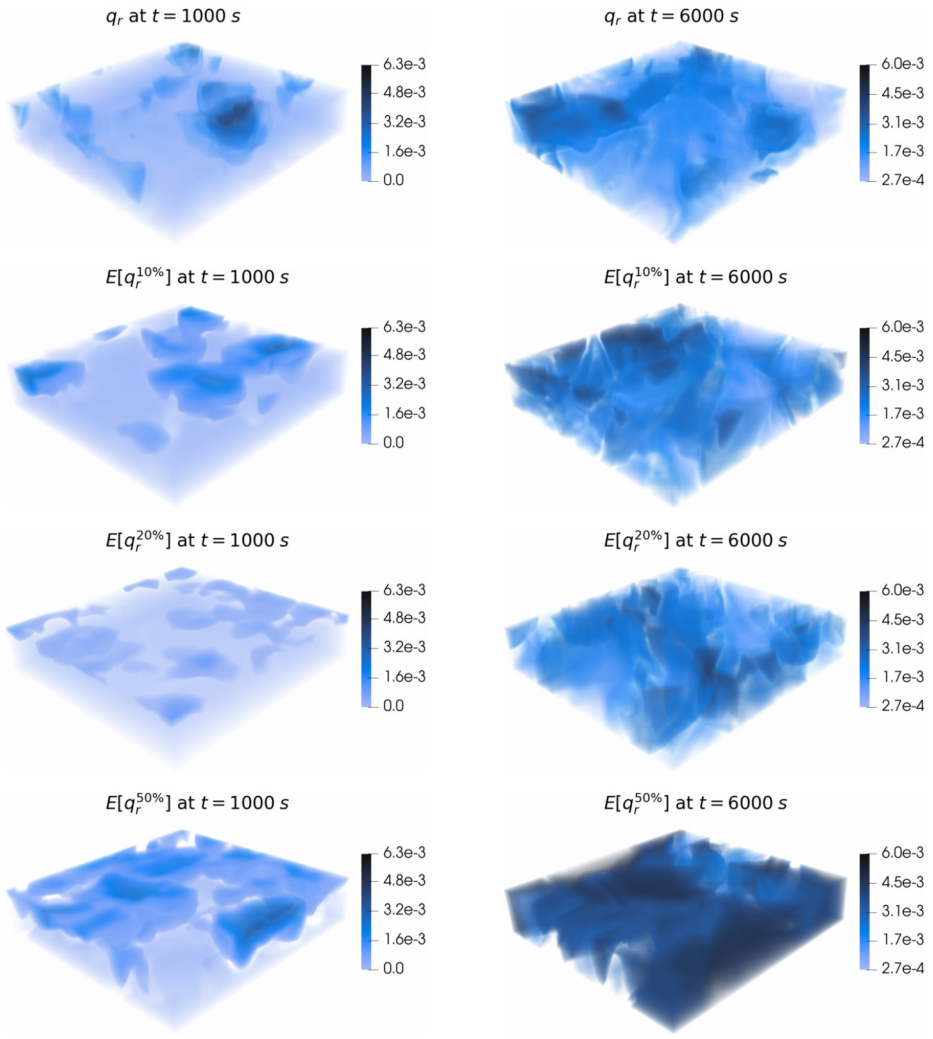

Fig. 18. Example 4.4: Expected value of the rain concentration q_r at times $t = 1000s$ and $6000s$ with 0%, 10%, 20% and 50% perturbations of the initial water vapor concentration.

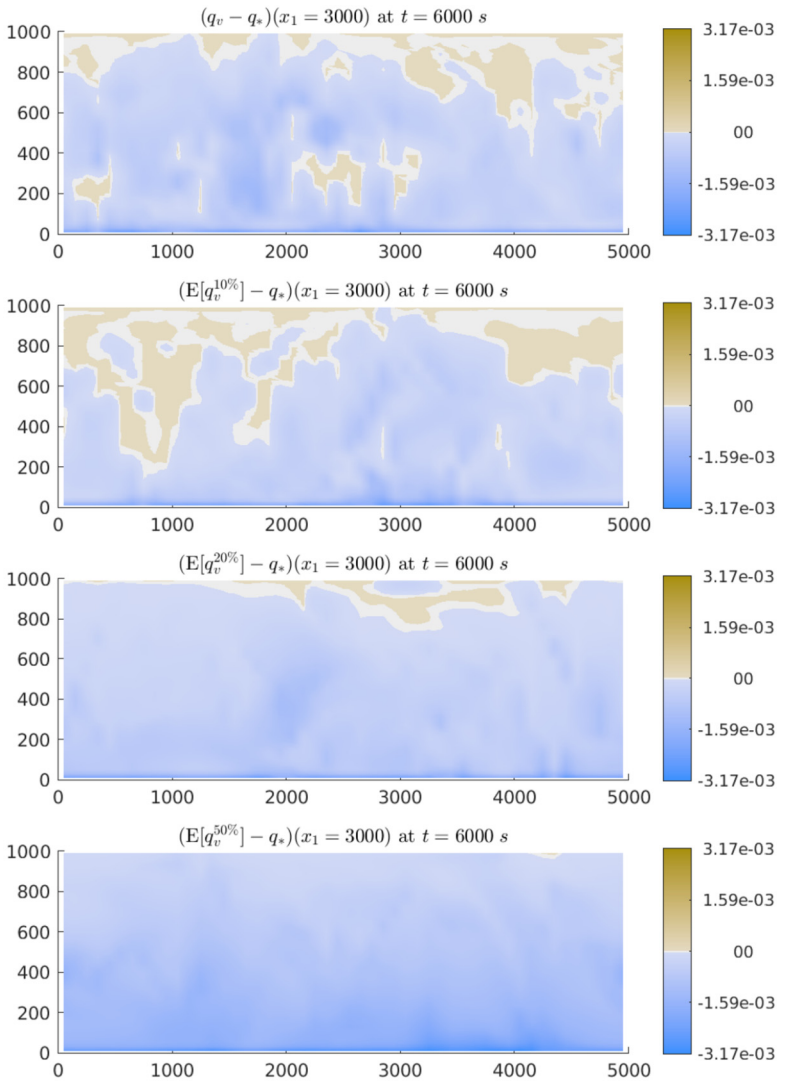

Fig. 19. Example 4.4: Slices of the difference between the water vapor and the saturation mixing ratio ($\mathbb{E}[q_v] - q_*$) along $x_1 = 3000$ at time $t = 6000s$ with 0%, 10%, 20% and 50% perturbations of the initial water vapor concentration.

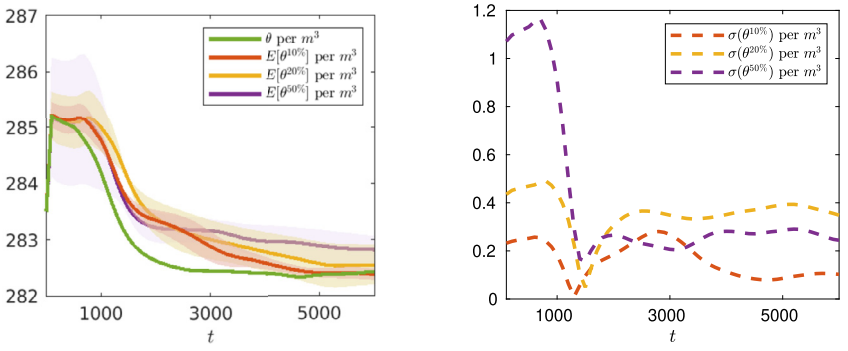

Fig. 20. Example 4.4: Time evolution of the expected values with their standard deviations for the potential temperature θ per m^3 (shaded region, left column) and standard deviations (right column) obtained using 0%, 10%, 20% and 50% perturbations of the initial data in q_v.

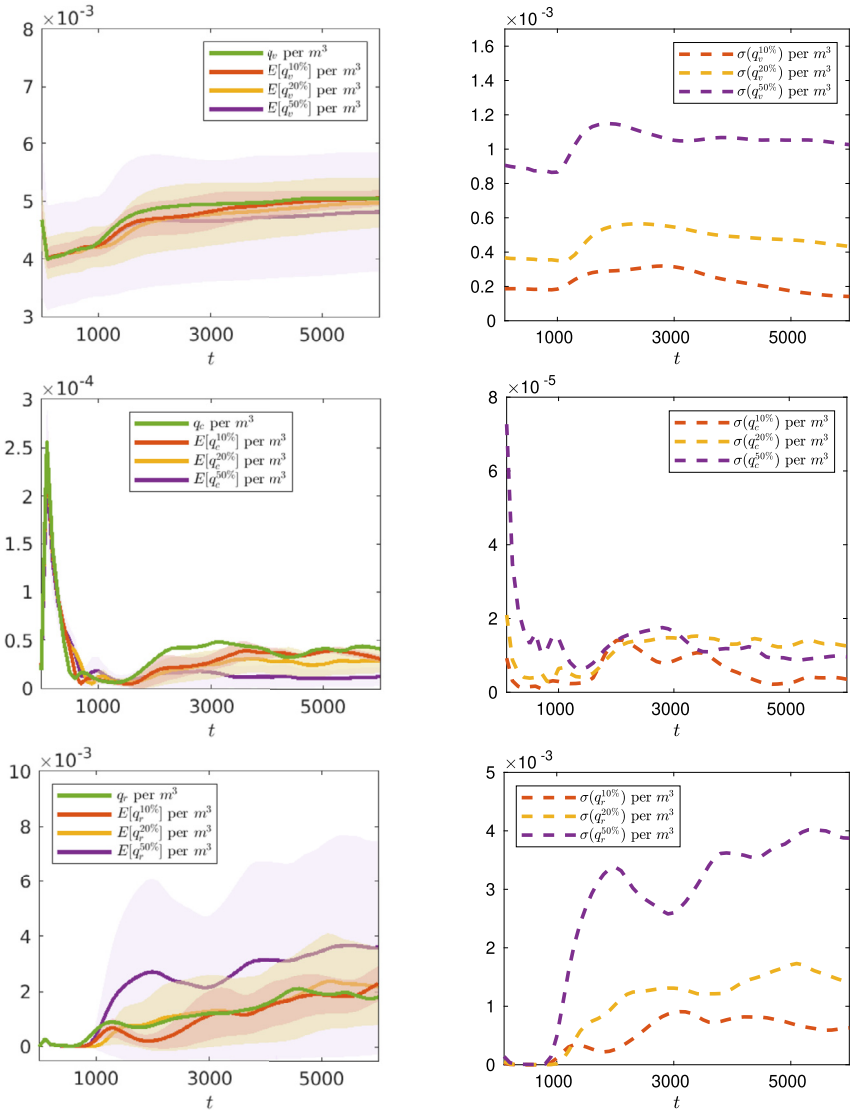

Fig. 21. Example 4.4: Time evolution of the expected values with their standard deviations for the cloud variables per m^3 (shaded region, left column) and standard deviations (right column) obtained using 0%, 10%, 20% and 50% perturbations of the initial data in q_v.

5. Conclusion

This paper is a continuation of our previous study on uncertainty propagation in atmospheric flows containing phase changes. In particular, we consider warm cloud dynamics of weakly compressible fluids. This model consists of a multiscale system of PDEs in which the macroscopic dynamics of the fluid is described by a weakly compressible Navier-Stokes system and the microscopic cloud dynamics is described by a system of convection-diffusion-reaction equations. We have extended the gPC-SG method from [8], where we considered a semi-random model with the deterministic macroscopic dynamics of the fluid coupled with the random microscopic cloud dynamics, to the case of a fully random multiscale system. To this end, we have first derived a system for the gPC coefficients and then presented a method we have used to numerically solve the resulting system. The latter is an extension of the numerical method developed in [8] and approximates the gPC coefficients for the dynamics of the fluid by an IMEX AP finite-volume method and the gPC coefficients for the cloud dynamics by an explicit finite-volume method with an enlarged stability region.

The aim of this work is to demonstrate the applicability, accuracy and efficiency of the gPC-SG method for atmospheric flows. Comprehensive studies of uncertainty propagation in these models considering different perturbation scenarios are left for a future work. Additionally, we will investigate the accuracy and performance of different uncertainty quantification methods, for instance, stochastic Galerkin, stochastic collocation and Monte Carlo method, in a review paper. Here, we have focused on numerical convergence and benchmark experiments as well as comparison with the results of the pre-

vious semi-random model presented in [8]. We have demonstrated that the gPC-SG method for the fully random model preserves the second-order spatial experimental convergence rate when the time increments are chosen according to the time step restriction and additionally exhibited an experimental exponential convergence rate in the stochastic space. This experimental convergence rate has been observed for both perturbation scenarios: uniform and normal distribution of the initial data perturbation. Additionally, we have studied the numerical solutions of the fully random cloud model for both the 2-D and 3-D Rayleigh-Bénard convection. By illustrating the behavior of clouds in different perturbed scenarios, we have demonstrated that perturbations of the initial conditions of cloud variables can crucially change the time evolution. The results have also exhibited a clear difference of the solutions of the semi- and fully random models in both the 2-D and 3-D Rayleigh-Bénard convection, which indicates that initial perturbations of cloud variables propagate to the Navier-Stokes equations and have a significant effect on the fluid variables. Our numerical study clearly demonstrates the applicability of the stochastic Galerkin method for the uncertainty quantification in complex atmospheric models and paves the path for more extensive practically relevant numerical studies.

We note that the presented method is not in general positivity preserving. As in many other numerical atmospheric and weather prediction models, the positivity of relevant quantities in our method is achieved by truncation at zero. It is, however, desirable to develop a provably positivity preserving extension of the proposed numerical method, which is essential not only for avoiding nonphysical values of the computed solution but also for ensuring the stability of the entire method. We leave this study for future work.

CRediT authorship contribution statement

A. Chertock: Conceptualization, Funding acquisition, Investigation, Methodology, Writing – original draft, Writing – review & editing. **A. Kurganov:** Conceptualization, Funding acquisition, Investigation, Methodology, Writing – original draft, Writing – review & editing. **M. Lukáčová-Medvid'ová:** Conceptualization, Funding acquisition, Investigation, Methodology, Supervision, Writing – original draft, Writing – review & editing. **P. Spichtinger:** Conceptualization, Funding acquisition, Investigation, Methodology, Writing – original draft. **B. Wiebe:** Conceptualization, Investigation, Methodology, Software, Visualization, Writing – original draft, Writing – review & editing.

Declaration of competing interest

The authors declare that they have no known competing financial interests or personal relationships that could have appeared to influence the work reported in this paper.

Data availability

The authors are unable or have chosen not to specify which data has been used.

Acknowledgement

The work of A. Chertock was supported in part by NSF grants DMS-1818684 and DMS-2208438. The work of A. Kurganov was supported in part by NSFC grants 12111530004 and 12171226, and by the fund of the Guangdong Provincial Key Laboratory Of Computational Science And Material Design (No. 2019B030301001). The work of M. Lukáčová-Medvid'ová, P. Spichtinger and B. Wiebe was supported by the German Science Foundation under the grant SFB/TRR 165 Waves to Weather (Project A2). M. Lukáčová-Medvid'ová and P. Spichtinger gratefully acknowledge the support of the Mainz Institute for Multiscale Modeling. M. Lukáčová-Medvid'ová thanks the Gutenberg Research College for supporting her research.

References

[1] A. Abdulle, A.A. Medovikov, Second order Chebyshev methods based on orthogonal polynomials, Numer. Math. 90 (1) (2001) 1–18.
[2] R. Abgrall, S. Mishra, Uncertainty quantification for hyperbolic systems of conservation laws, in: Handbook of Numerical Methods for Hyperbolic Problems, in: Handb. Numer. Anal, vol. 18, Elsevier/North-Holland, Amsterdam, 2017, pp. 507–544.
[3] R. Abgrall, S. Tokareva, The stochastic finite volume method, in: Uncertainty Quantification for Hyperbolic and Kinetic Equations, in: SEMA SIMAI Springer Ser., vol. 14, Springer, Cham, 2017, pp. 1–57.
[4] U.M. Ascher, S.J. Ruuth, R.J. Spiteri, Implicit-explicit Runge-Kutta methods for time-dependent partial differential equations, in: Special Issue on Time Integration, Amsterdam, 1996, Appl. Numer. Math. 25 (2–3) (1997) 151–167.
[5] G. Bispen, IMEX finite volume methods for the shallow water equations, dissertation, Johannes Gutenberg-Universität Mainz, 2015.
[6] G. Bispen, M. Lukáčová-Medvid'ová, L. Yelash, Asymptotic preserving IMEX finite volume schemes for low Mach number Euler equations with gravitation, J. Comput. Phys. (2017).
[7] G.H. Bryan, J.M. Fritsch, A benchmark simulation for moist nonhydrostatic numerical models, Mon. Weather Rev. 130 (2002) 2917–2928.
[8] A. Chertock, A. Kurganov, M. Lukáčová-Medvid'ová, P. Spichtinger, B. Wiebe, Stochastic Galerkin method for cloud simulation, Math. Clim. Weather Forecast. 5 (1) (2019) 65–106.
[9] R.M. Davies, F.J. Taylor, The mechanism of large bubbles rising through extended liquids and through liquids in tubes, Proc. Royal Soc. Lond. A 200 (1950) 375–390.
[10] B. Després, G. Poëtte, D. Lucor, Robust uncertainty propagation in systems of conservation laws with the entropy closure method, in: Uncertainty Quantification in Computational Fluid Dynamics, in: Lect. Notes Comput. Sci. Eng., vol. 92, Springer, Heidelberg, 2013, pp. 105–149.

[11] H.C. Elman, C.W. Miller, E.T. Phipps, R.S. Tuminaro, Assessment of collocation and Galerkin approaches to linear diffusion equations with random data, Int. J. Uncertain. Quantificat. 1 (1) (2011) 19–33.
[12] E. Feireisl, M. Lukáčová-Medvid'ová, Convergence of a stochastic collocation finite volume method for the compressible Navier-Stokes system, 2021.
[13] E. Feireisl, M. Lukáčová-Medvid'ová, Statistical solutions for the Navier-Stokes-Fourier system, 2022.
[14] M. Frank, J. Kusch, J. Wolters, Entropy–based methods for uncertainty quantification of hyperbolic conservation laws, in: SEMA SIMAI Springer Series, Springer International Publishing, 2021, pp. 29–56.
[15] E. Hairer, G. Wanner, Solving Ordinary Differential Equations. II. Stiff and Differential-Algebraic Problems, second ed., Springer Series in Computational Mathematics, vol. 14, Springer-Verlag, Berlin, 1996.
[16] O. Le Maître, M.T. Reagan, B. Debusschere, H.N. Najm, R.G. Ghanem, O.M. Knio, Natural convection in a closed cavity under stochastic non-Boussinesq conditions, SIAM J. Sci. Comput. 26 (2) (2004) 375–394.
[17] O.P. Le Maître, O.M. Knio, Spectral Methods for Uncertainty Quantification, Springer, Netherlands, 2010.
[18] O.P. Le Maître, O.M. Knio, H.N. Najm, R.G. Ghanem, A stochastic projection method for fluid flow. I. Basic formulation, J. Comput. Phys. 173 (2) (2001) 481–511.
[19] O.P. Le Maître, M.T. Reagan, H.N. Najm, R.G. Ghanem, O.M. Knio, A stochastic projection method for fluid flow. II. Random process, J. Comput. Phys. 181 (1) (2002) 9–44.
[20] X. Ma, N. Zabaras, An adaptive hierarchical sparse grid collocation algorithm for the solution of stochastic differential equations, J. Comput. Phys. 228 (8) (2009) 3084–3113.
[21] A.A. Medovikov, Dumka 3 code, available at http://dumkaland.org/.
[22] A.A. Medovikov, High order explicit methods for parabolic equations, BIT Numer. Math. 38 (2) (1998) 372–390.
[23] M.P. Pettersson, G. Iaccarino, J. Nordström, Polynomial Chaos Methods for Hyperbolic Partial Differential Equations, Springer International Publishing, 2015.
[24] G. Poëtte, B. Després, D. Lucor, Uncertainty quantification for systems of conservation laws, J. Comput. Phys. 228 (7) (2009) 2443–2467.
[25] M. Taylor, Riemann Integrable Functions on a Compact Measured Metric Space, Functional Analysis Course, Univ. of North Carolina, 2021.
[26] J. Tryoen, O. Le Maître, M. Ndjinga, A. Ern, Intrusive Galerkin methods with upwinding for uncertain nonlinear hyperbolic systems, J. Comput. Phys. 229 (18) (2010) 6485–6511.
[27] X. Wan, G.E. Karniadakis, Long-term behavior of polynomial chaos in stochastic flow simulations, Comput. Methods Appl. Mech. Eng. 195 (41–43) (2006) 5582–5596.
[28] J.A.S. Witteveen, A. Loeven, H. Bijl, An adaptive stochastic finite elements approach based on Newton-Cotes quadrature in simplex elements, Comput. Fluids 38 (6) (2009) 1270–1288.
[29] D. Xiu, Numerical Methods for Stochastic Computations: A Spectral Method Approach, Princeton University Press, Princeton, NJ, 2010.
[30] D. Xiu, J.S. Hesthaven, High-order collocation methods for differential equations with random inputs, SIAM J. Sci. Comput. 27 (3) (2005) 1118–1139 (electronic).
[31] D. Xiu, G.E. Karniadakis, The Wiener-Askey polynomial chaos for stochastic differential equations, SIAM J. Sci. Comput. 24 (2) (2002) 619–644 (electronic).